Scale resolving simulations of a high-temperature turbulent jet in a cold crossflow: Comparison of two approaches

Romain Paysant, Emmanuel Laroche, Julien Troyes, David Donjat, Pierre Millan, Pierre Buet

Scale resolving simulations of a high-temperature turbulent jet in a cold crossflow: comparison of two approaches

Romain Paysant[a,*], Emmanuel Laroche[b], Julien Troyes[b], David Donjat[b], Pierre Millan[b], Pierre Buet[a]

[a] *Airbus Helicopters S.A.S, Aéroport International Marseille Provence, Marignane, France*

[b] *ONERA/DMPE, Université de Toulouse, 2 avenue Edouard Belin, Toulouse, France*

Abstract

A high-temperature turbulent jet in a cold crossflow is investigated with the help of two scale-resolving simulation approaches. This work aims at improving the methodologies used to predict the thermal footprint of exhaust gases issuing from helicopter engines onto the fuselage. Specific attention is brought to the capability of scale resolving simulations to correctly reproduce flow dynamics and turbulent mixing. Mean flow features, turbulent quantities and temperature fields are compared and validated against wind tunnel test measurements. In addition, the present work highlights the importance of synthetic turbulence injection at pipe inlet to obtain a fair prediction of both flow dynamics and temperature field.

Keywords: jet in crossflow, CFD, RANS/LES, turbulence

Notations

*romain.paysant@gmail.com

V_R = velocity ratio

C_R = blowing ratio

D = pipe internal diameter

H = height of the computational domain

T_j = jet static temperature

T_{cf} = crossflow static temperature

ρ_j = jet density

ρ_{cf} = crossflow density

V_j = mean jet velocity

V_{cf} = mean crossflow velocity

Pr_t = turbulent Prandtl number

R = momentum flux ratio

Re_j = jet Reynolds number

Re_{cf} = crossflow Reynolds number

U = mean flow velocity in the x direction

V = mean flow velocity in the y direction

W = mean flow velocity in the z direction

$\vec{V}$ = mean velocity vector

$\|\vec{V}\|$ = mean velocity magnitude

k = turbulent kinetic energy

ω = specific dissipation rate

ε = turbulent dissipation

ν_t = turbulent (or eddy) viscosity

θ = normalized mean temperature

α_t = turbulent diffusivity

$\overline{u_i' u_j'}$ = Reynolds stress tensor

$\overline{u_i' T'}$ = turbulent heat flux vector

1. Introduction

Jets in crossflow have been extensively studied and are still at the heart of many research topics. The strong interest in this kind of flow has led to countless publications, as better understanding the physics of jets in crossflows is of primary interest for many industrial and natural applications Margason (1993); Mahesh (2013); Karagozian (2014). Over time, the scope of jets in crossflow applications has grown steadily. First studies were mainly focused on trajectory and dispersion of pollutants and plumes issuing from smokestacks, volcanoes or effluents Sutton (1932); Bosanquet and Pearson (1936). Later on, jets in crossflows have been studied to better understand pitch-up effect caused by lifting jets of Vertical and/or Short Take-Off and Landing (V/STOL) aircrafts during transitional flight phases Carter (1969); Gentry Jr and Margason (1968). This kind of flow is also of primary interest in a gas turbine context as it is involved in film cooling, dilution jets and fuel injection Hale et al. (2000); Eriksen and Goldstein (1974); Arroyo-Callejo et al. (2016); Ivanova et al. (2009). With the increasing use of numerical simulations, many recent studies have been focused on the ability of Computational Fluid Dynamics (CFD) methods to simulate such flows Mahesh

(2013).

The present work investigates the capability of aerothermal CFD simulations to correctly reproduce trajectory and mixing of exhaust gases ejected by helicopters engines in order to support design. Actually, exhaust gases ejected by helicopters engines can be assimilated to jets in crossflow as they interact with a complex flowfield composed of rotor downwash, relative wind and ground effect for some flight cases. This jet in crossflow configuration is characterized by a strong temperature gradient between the jet and the crossflow as exhaust gases are ejected at temperatures close to 600°C to 700°C. Their interaction with the external flowfield can lead to thermal issues such as the overheating of structural parts or external equipment and the reingestion of hot gases through engines and avionics bays air intakes. Hence, being able to predict exhaust gases trajectory and their turbulent mixing with the surrounding flow is critical for design purpose.

Several studies have been carried out so far to investigate the capability of various turbulence modeling approaches to correctly simulate jets in crossflow. It has been shown that standard statistical turbulence models are not able to correctly reproduce the turbulent mixing occurring between the jet and the crossflow Ivanova et al. (2009); Bézard et al. (2012); Galeazzo et al. (2013); Prause et al. (2016); Rusch et al. (2008).

Conversely, many studies have evidenced that scale resolving approaches such as Large Eddy Simulations (LES) or hybrid RANS/LES methods provide fair predictions of both dynamics and thermal field. For instance, Yuan *et al.* Yuan et al. (1999) simulated jets in crossflow at velocity ratios $V_R = V_j/V_{cf}$ of 2.0 and 3.3 and $Re_{cf} = DV_{cf}/\nu = 1050$ and 2100 using the

LES approach. Simulated profiles of the mean velocity magnitude and its associated fluctuations were in good agreement with measurements. However, the comparison was limited to the centreplane. Zhang & Yang Zhang and Yang (2017a,b) also used LES simulations to investigate flow dynamics and mixing of jets in crossflow at two different velocity ratios (2.0 and 4.0) in both steady and oscillating crossflow. Similarly, Denev *et al.* Denev et al. (2009) performed LES simulations to study the influence of swirl on the turbulent mixing of a passive scalar injected into the jet. In these studies, the LES approach was validated on a benchmark configuration for which experimental data are available. The authors then successfully used LES calculations to investigate the influence of different parameters on flow behaviour and to provide additional information not available experimentally. Prause *et al.* Prause et al. (2016) compared LES, SAS-SST, URANS-SST and RANS-SST approaches for two jets in crossflow at $R = (\rho_j V_j^2/\rho_{cf} V_{cf}^2)^{1/2} = 0.7$ and 1.41 and $Re_j = DV_j/\nu = 20\,500$ and $82\,000$ respectively. They noticed a good agreement between tests and LES results. The SAS-SST approach provides results which are in good agreement with LES ones in the far field. However, they observed that the turbulence model does not switch to its scale resolving mode up to $X/D = 1.0$ delaying the upstream shear layer roll-up. On the contrary, URANS-SST does not provide improved results over RANS-SST. It is worth mentioning that all above studies dealt with jet in crossflow configurations for which jet and crossflow are at the same temperature or density. Jouhaud *et al.* Jouhaud et al. (2007) performed LES simulations on a slightly heated jet in crossflow at low momentum flux ratio $R = 0.9$ and $Re_{cf} = DV_{cf}/\nu = 93\,900$. On the one hand, they demon-

strated that profiles of film cooling effectiveness η are well predicted by both RANS and LES approaches within the centreplane. On the other hand, they showed that the RANS approach is not capable of predicting spanwise jet spreading/diffusion while LES provides fair results. However, their results were limited to moderate temperature difference between jet and crossflow ($\Delta T = 70\,\mathrm{K}$). In addition, given the low value of R, the jet remained attached to the wall. Duda *et al.* Duda et al. (2011); Duda (2012); Duda et al. (2014) also obtained good results using ZDES and SAS approaches for a low momentum flux ratio jet in crossflow at moderate ΔT. Ivanova *et al.* Ivanova et al. (2009) carried out SAS-SST and URANS-SST simulations on a heated jet in crossflow configuration at $R = 6.46$. The temperature difference between jet and crossflow was of 152 K (crossflow is heated, jet is cold). Their results show that the SAS approach resolves a larger part of the turbulent spectrum compared to the URANS approach with the same mesh. They noticed that the additional production term in the transport equation of the specific dissipation ω in the SAS approach was active in a large part of the domain leading to a reduction of ν_t and less damping of small turbulent structure with respect to URANS method. Nevertheless, they did not notice significant discrepancies between the two approaches on large scale structures and velocity profiles. On the contrary, both approaches provide a significant improvement over RANS simulations which contrasts with the findings of other studies. However, they highlighted the necessity of resolving large scale structures for proper prediction of this kind of flow like several other studies. Rusch *et al.* Rusch et al. (2008) carried out experiments and performed scale resolving simulations on a hot jet in crossflow ($T_j \approx 500°\mathrm{C}$) at $R = 2.33$. They

used URANS-SST, $k-\sqrt{k}L$-SAS and DES methods. They did not notice significant improvement with the use of the URANS-SST method compared to SST-RANS. DES approach provides better results but they underline that mesh was too coarse and it remains in RANS mode in a large part of the domain. The best results were obtained with the $k-\sqrt{k}L$-SAS approach. The SAS solution is in good agreement with measurements in the far field but shows some issues in the near field. The authors suggested two explanations for this behaviour: a delayed switching towards scale resolving mode and the underlying isotropic eddy viscosity hypothesis which cannot capture the strong anisotropy of turbulence in the near field due to strong streamlines curvature. However, involved velocities are small ($V_j = 2.71\,\mathrm{m/s}$ and $V_{cf} = 0.73\,\mathrm{m/s}$) and jet develops in a confined environment. Although this bibliography review is obviously not exhaustive, one can see that studies available in the literature have not investigated the ability of scale resolving simulation methods to predict jet in crossflow involving a high-temperature difference between jet and crossflow as it is the case in rotorcraft application. Therefore, the present paper aims at providing a better understanding of the simulation of such flows.

The article is organized as follows. First, the experimental and numerical setups are introduced. Then simulations results and measurements are compared to validate both dynamics and thermal aspects. The suitability of the gradient diffusion hypothesis to model the turbulent heat flux in the present flow is then discussed. Finally, the influence of synthetic turbulence injection at the pipe inlet is discussed.

2. Experiments

A detailed experimental database has been generated for two jets in crossflow configurations whose blowing ratio, momentum flux ratio and temperature difference are representative of a helicopter application. The main characteristics of these two jets in crossflow are presented in Table 1:

	T_j	C_R	R	ρ_j/ρ_{cf}	D
High-temperature jet	400°C	1.54	2.33	0.432	40 mm
Moderate temperature jet	60°C	1.54	1.62	0.88	40 mm

Table 1: Main characteristics of the jets in crossflow studied experimentally.

The experiments were conducted within F2 wind tunnel located at ONERA Fauga-Mauzac Center. The ONERA F2 wind tunnel is a large research-type low speed wind tunnel. A schematic view of the installation is presented in Figure 1.

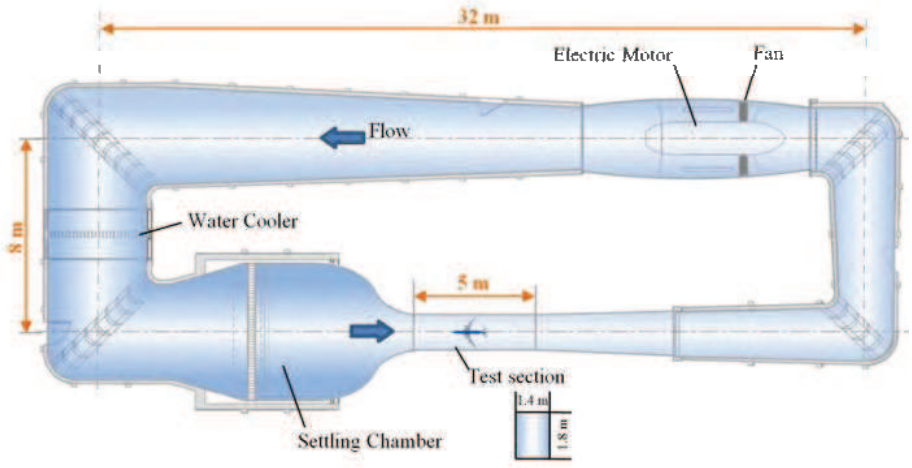

Figure 1: Schematic view of ONERA F2 wind tunnel.

The experimental setup is presented in Figure 2.

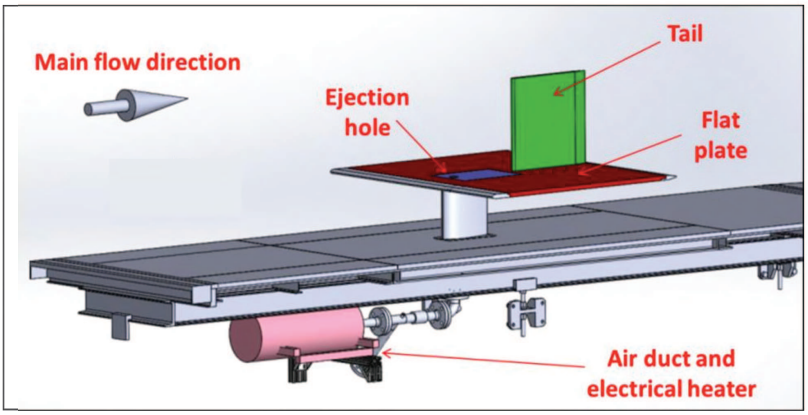

Figure 2: Visualization of the experimental setup.

The jet is produced by a round pipe of internal diameter $D = 40\,\text{mm}$. The pipe is flush-mounted onto a flat plate (red part in Figure 1) with an angle of 90°. The flat plate being parallel to wind tunnel floor, the jet is therefore ejected perpendicularly to the crossflow. A fairing with a symetric airfoil shape is added around the pipe between the flat plate and the wind tunnel floor. This fairing limits flow disturbance due to the presence of the pipe. In addition, it is filled with an insulating material assuring the thermal insulation of the pipe. A vertical fin (green part in Figure 1) is located $10D$ downstream to investigate the interaction of the jet with a part of structure. The role of this vertical fin is to mimic the interaction of the jet with an helicopter vertical tail fin. To produce the jet, the pipe is fed with hot air pressurized at 8 bar and heated up by two 16 kW Leister electrical heaters. The flow leaving the pipe exhibits a fully developed velocity profile in the absence of crossflow. To obtain the aforementioned velocity profile, a LAWS flow conditioner has been placed inside the pipe downstream of the 90°

elbow in the blowing circuit. Jet mass flow rate is measured with a Coriolis flowmeter located upstream the heaters. The total temperature of the hot jet is controlled slightly upstream pipe outlet. In addition, Laser Doppler Velocimetry (LDV) and thermocouples measurements have been performed close to the pipe outlet to verify flow symetry and temperature uniformity in the absence of crossflow. Crossflow conditions are defined by a freestream velocity V_{cf} set to 30 m/s and a static temperature T_{cf} maintained to 20°C. As a result, the crossflow Reynolds number Re_{cf} based on jet exit diameter is about 80 000. Two jets in crossflow (Table 1) were investigated by modifying blowing conditions.

For both jets in crossflow, a complete characterisation of flow dynamics has been performed. Stereo Particle Image Velocimetry (S-PIV) was used to measure mean components and RMS fluctuations of the velocity field in several longitudinal planes. In addition, LDV measurements have been performed to accurately characterise flow dynamics at the pipe outlet and within the turbulent boundary layer developing over the flat plate. A boundary layer thickness of about 3 to 4 mm was measured $4D$ upstream the pipe outlet. Regarding thermal aspects, time-averaged temperatures within jet plume have been measured with a moving thermocouple rake over a distance ranging from $0.5D$ to $3D$ downstream pipe outlet. In addition, Background Oriented Schlieren (BOS) technique was applied to measure 2D and 3D density fields and infra-red thermography measurements were performed over the fin surface. A detailed presentation and analysis of these wind tunnel tests can be found in a companion paper Donjat et al. (2021) (submitted, waiting for acceptation).

3. Numerical setup

Scale-resolving simulations have been carried out on the high-temperature jet in crossflow configuration investigated during the ONERA F2 wind tunnel tests. This configuration is referred to as "high-temperature jet" in Table 1. The work being carried out jointly between Airbus Helicopters and ONERA, two Computational Fluid Dynamics (CFD) solvers have been used in the present study. On the one hand, ANSYS Fluent 2019R2 has been used as it is currently the reference software within Airbus Helicopters for aerothermal topics. On the other hand, ONERA CEDRE v.7.1.1 has been used as it is the reference software within ONERA for multiphysics applications. Both softwares rely on an unstructured finite-volume method to solve Navier-Stokes equations. The numerical setup used for the simulations is described in the following sections.

3.1. Computational domain

The computational domain used for all calculations is presented in Figure 3. The origin of the coordinate system was chosen to be at the center of pipe outlet. Wind tunnel and pipe inlets are located $4D$ away from this point. Top and sidewalls locations are chosen such that the flow is not influenced by confinement effects. The top wall is located at a height $H = 10D$ above the flat plate which corresponds to the height of the fin used in the experiments (not included in the simulations presented in this paper). Infra-red acquisitions performed over the fin surface have shown that jet impingement on the fin occurs at an altitude significantly lower than H. Sidewalls are located $2H$ apart from each other which corresponds to the experimental flat plate

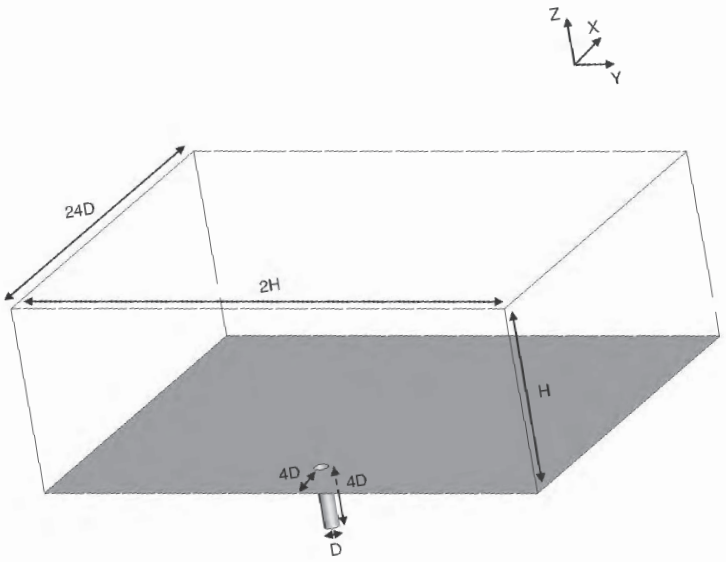

Figure 3: Visualization of the computational domain.

span and the actual location of wind tunnel walls. All walls of the computational domain are modelled using an adiabatic wall condition. Top and sidewalls being far from the area of interest, slip conditions are applied to avoid mesh refinement close to the wall and reduce mesh size. No-slip conditions are therefore only used for pipe and flat plate walls. On the one hand, uniform temperature as well as profiles of mass flux and turbulent quantities are specified at the wind tunnel inlet boundary condition. These profiles have been obtained by LDV measurements $4D$ upstream jet ejection. As for the pipe, profiles of total pressure, total temperature and turbulent quantities corresponding to a fully developed pipe flow are prescribed at the pipe inlet. These profiles are extracted from a preliminary steady-state RANS calculation of a periodic pipe. Finally, a uniform static pressure condition set to 1013.25 hPa is applied at the outlet of the fluid domain which is located $20D$

downstream of the jet ejection location.

3.2. Meshes

As ANSYS Fluent and ONERA CEDRE rely on different numerical methods, two different meshes have been generated in accordance with the best practice guidelines of each code. The two meshes are unstructured grids composed of tetrahedral and prismatic elements. Prism layers were only grown from pipe wall and flat plate as slip conditions are applied to the other walls. The main characteristics of both meshes are detailed in the following paragraphs.

The mesh used for ANSYS Fluent calculations has a maximum cell size of $\Delta x = 4\,\text{mm}$ within the whole fluid domain where Δx is a characteristic length scale of the elements. The mesh is refined close to the pipe outlet with the help of two nested refinement areas. Along the vertical direction, the refinement areas extend from the wall to an altitude that loosely follow the upper boundary of the jet obtained with a precursor RANS calculation. Within the larger refinement area, which extends from $X/D = -1.25$ to $X/D = 10.0$ in the longitudinal direction and from $Y/D = -2.5$ to $Y/D = 2.5$ in the transverse direction, the maximum cell size is set to $\Delta x = 2\,\text{mm}$. Within the smaller refinement area, which extends from $X/D = -1.25$ to $X/D = 1.5$ in the longitudinal direction and from $Y/D = -1.5$ to $Y/D = 1.5$ in the transverse direction, the maximum cell size is set to $\Delta x = 1\,\text{mm}$. In addition, the mesh is refined close to the wall with the use of 22 prism layers. In the vicinity of the wall, the first cell height is set to $10\,\mu\text{m}$ leading to $y^+ \leq 1$ everywhere in the domain. A growing ratio of 1.2 is specified to guarantee a smooth transition between prism layers and a good resolution of

the boundary layer. The final mesh has a size of about 42 million elements.

The mesh used for ONERA CEDRE calculations retains the same construction logic based on nested refinements boxes. For this mesh, refinement boxes are cubic for simplicity. All boxes have their upstream face located at $X/D = -1.0$ and are centered along $Y/D = 0$. The first refinement box, whose sides have a length of $2D$, prescribes a maximal element length scale of $\Delta x = 0.5\,\text{mm}$ in its volume. The second one features a side length of $4D$ and prescribes a maximal element length scale of $\Delta x = 1\,\text{mm}$. The larger one have a side length of $6D$ and limits the element length scale to $\Delta x = 2.5\,\text{mm}$ within its volume. The same refinement than the other mesh is used at the wall. The resulting mesh has a size of about 53 million elements.

A proper grid independence study has not been carried out in the present work due to the prohibitive computational cost of such simulations. However, it is assumed that both meshes are fine enough to correctly capture flow dynamics and mixing. Therefore, it is assumed that the results dependence to the grid is not of first order. Accordingly, the comparisons of SAS and LES simulations (carried out in the following sections) reveal that the two approaches give very similar results despite the different treatment of the modelled part of the turbulent spectrum. This observation supports the weak dependence of the results to the grid.

3.3. Solver settings

The pressure-based solver has been used for the SAS-SST calculations carried out with ANSYS Fluent. Solver settings have been defined according to ANSYS Fluent best practice guidelines for scale resolving simulations detailed in Menter (2015). Pressure-velocity coupling is performed with the

help of the SIMPLEC scheme Van Doormaal and Raithby (1984). Second order upwind scheme was selected for spatial discretization of all transported quantities except momentum for which the central difference scheme is used (the recommended Bounded Central Differencing scheme turned out to be too dissipative for this flow configuration). The least squares cell based method was used for gradients computation. An implicit second-order accurate discretization scheme has been used for time discretization. A fixed time-step $\Delta t = 5.10^{-6}$ s has been used leading to a maximal cell convective Courant number of 3 in the fluid domain.

As mentioned previously, the LES computations were carried out with the multi-physics code CEDRE Refloch et al. (2011). Solver settings have been defined in accordance with ONERA's experience in simulating similar kind of flows. The spatial discretization scheme is a 2^{nd} order k-exact method Haider et al. (2018). An HLLC Riemann solver was selected for flux calculation. Gradients computation is performed with a least squares method. The time integration is performed with an implicit 2^{nd} order Runge-Kutta scheme associated with a GMRES type linear system solver. Similarly to the SAS-SST calculations, the time step was set to $\Delta t = 5.10^{-6}$ s leading to the same maximal cell convective Courant number of 3 in the fluid domain.

3.4. Turbulence modelling

Two turbulence modelling approaches have been investigated in this study. On the one hand, calculations performed with ANSYS Fluent used the Scale-Adaptive Simulation (SAS) approach coupled to a $k - \omega$ SST turbulence model as proposed by Menter & Egorov Menter and Egorov (2010). This approach will be called SAS-SST in the rest of the paper. On the other

hand, calculations carried out with CEDRE used the Large Eddy Simulation approach with a standard Smagorinsky subgrid scale model. A constant value $C = 0.18$ was chosen for the Smagorinsky model and the van Driest damping function was used at the wall. These two turbulence modelling approaches being classical ones and well documented in the literature they will not be detailed here for conciseness purpose. The reader is referred to Sagaut *et al.* Sagaut et al. (2013) and previously cited papers for a comprehensive review of these approaches.

3.5. Convergence monitoring

Convergence of all calculations has been carefully monitored. Time step convergence (or inner convergence) has been checked by placing virtual sensors within the area of interest and plotting the evolution of several variables for all inner iterations within a time step. For ANSYS Fluent calculations, inner convergence is achieved when residuals have decreased by two orders of magnitude within a time step. Time step convergence is reached after 7 inner iterations once the transient phase has been passed. For all calculations, the global convergence has been checked by plotting averaged signals from previously mentioned sensors and ensuring that mean values are stabilised. In addition, global comparisons of averaged and root mean squares (RMS) quantities in different slices for two distinct time steps have been undertaken and differences turned out to be negligible. For illustration, an example of such comparison undertaken on the mean static temperature fields in three transverse planes is presented in Figure 4. Differences are less than 1K on mean static temperature fields between the two simulation times.

This has led to the definition of a convergence criterion based on the sim-

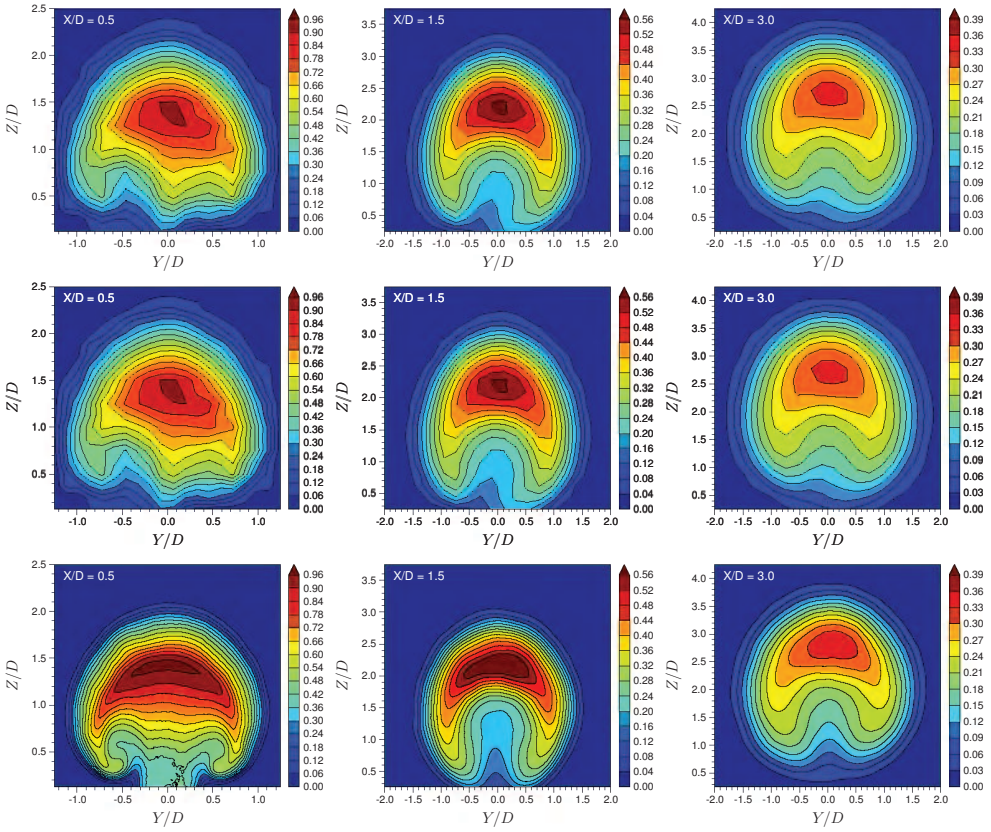

Figure 4: Normalized mean static temperature fields $\theta = (T - T_{cf})/(T_j - T_{cf})$ in three transverse planes (from left to right: $X/D = 0.5$, 1.5 and 3.0) for two simulation times $t_{sim} = 0.25\,\mathrm{s}$ and $t_{sim} = 0.5\,\mathrm{s}$ (ANSYS Fluent SAS-SST).

ulated time corresponding to $t_{sim} \geq 0.25\,\mathrm{s}$. This criterion has been applied to all calculations presented in this paper. It is worth noting that this criterion is peculiar to the present calculation case and is likely to be overestimated as no proper study has been undertaken to accurately determine the minimum simulation time required.

4. Results

In this section, computational results and experimental measurements are compared to validate both dynamics and thermal aspects of simulated flow fields. The two simulation approaches discussed in this section include synthetic turbulence injection at pipe inlet as results were found to be more

relevant in this case. A discussion dedicated to the influence of pipe inlet conditions is carried out in section 5 of the present paper. In the present study, two methods of synthetic turbulence generation have been used as CEDRE and Fluent rely on different approaches. The Synthetic Eddy Model (SEM) method proposed by Jarrin *et al.* Jarrin et al. (2006); Jarrin (2008); Jarrin et al. (2009) has been used for LES calculations carried out with CEDRE while the Synthetic Turbulence Generator (STG) proposed by Shur *et al.* Shur et al. (2014) has been used for SAS-SST calculations performed with ANSYS Fluent. Therefore, the two approaches will be called SAS-SST + STG and LES + SEM in the rest of this paper.

4.1. Instantaneous fields

In order to assess quantitatively the proper RANS to LES transition in the SAS-SST + STG simulation, a view of the turbulent to molecular viscosity ratio in the centreplane $Y/D = 0$ is presented in Figure 5.

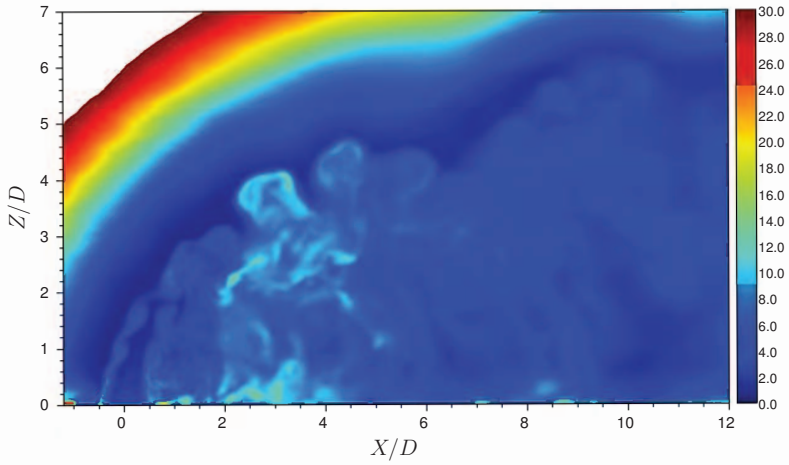

Figure 5: Viscosity ratio ν_t/ν in the centreplane $Y/D = 0$ for the SAS-SST + STG calculation.

Large values of ν_t/ν are caused by high levels of eddy viscosity ν_t which prevent the formation of resolved turbulence leading therefore to a RANS-like solution. As ν_t/ν ratio decreases (under the action of the source term added to the ω transport equation in the case of the SAS-SST approach) a larger part of the turbulent spectrum is being resolved. Figure 5 shows that ν_t/ν levels are low in the area of interest which demonstrates that flow turbulence is mainly time-resolved in this region. One can also see that the turbulence within the incoming boundary layer developing over the flat plate is mainly modelled upstream $X/D = -1.0$ where it remains attached to the wall. At $X/D = -1.0$, viscosity ratio exhibits an abrupt drop which marks the boundary layer separation under the action of the adverse pressure gradient induced by jet blockage effect. Within jet region, one can see that viscosity ratio increases past $X/D = 2.0$ due to mesh coarsening. However, the levels remain small compared to the ones observed within RANS-like areas (within the incoming boundary layer developing over the flat plate upstream $X/D = -1.0$ where it remains attached to the wall). Therefore, it can be assumed that flow turbulence is still mainly resolved.

Instantaneous visualisations of the temperature field in the centreplane from SAS-SST + STG and LES + SEM calculations are presented in Figure 6. Both plots evidence mixing layers roll-up caused by the development of a Kelvin-Helmholtz instability on either windward and lee sides of the jet. One can see that shear-layer roll-up occurs closer to the pipe outlet in the LES calculation. This is especially true for the downstream shear layer. In addition, the LES resolves a larger part of the turbulence spectrum than the SAS-SST. This is highlighted by the presence of finer-scale turbulence

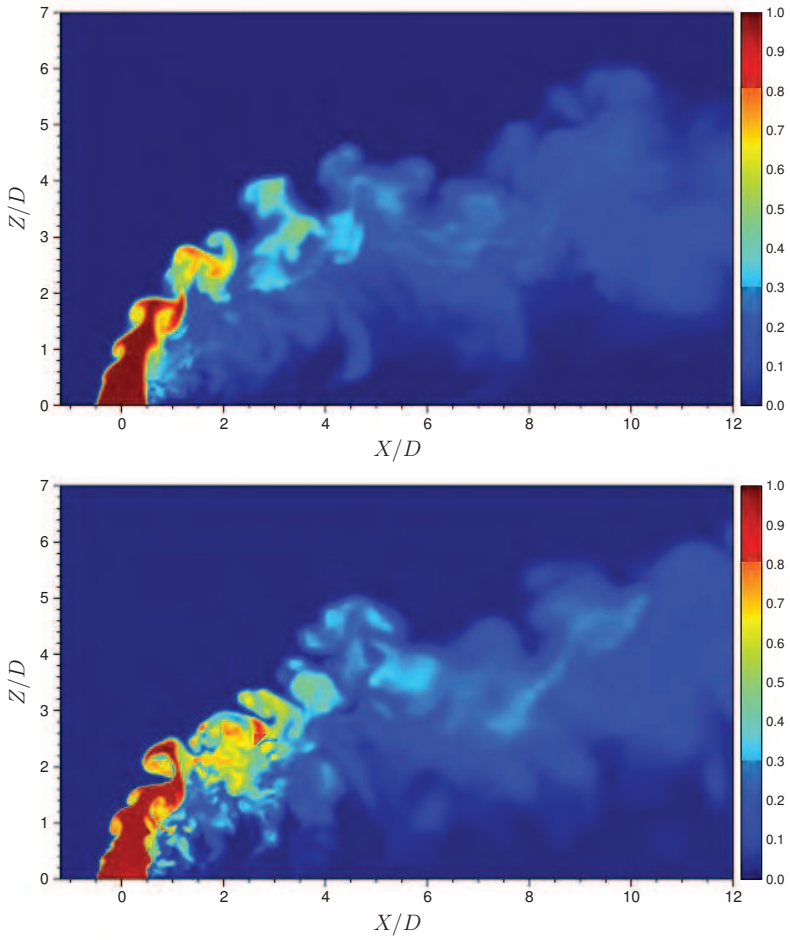

Figure 6: Instantaneous fields of normalized temperature $\theta = (T - T_{cf})/(T_j - T_{cf})$ in the centreplane $Y/D = 0$. SAS-SST + STG (top) and LES + SEM (bottom).

structures in the instantaneous temperature field computed by the LES.

4.2. Jet trajectory

Multiple definitions of jet trajectory can be found in the literature which requires to be cautious when comparing results to other studies or correlations. In the present paper, the jet trajectory is defined by the maxima of

mean longitudinal velocity U in the centreplane $Y/D = 0$. The experimental jet trajectory is obtained by extracting these local U maxima from Particle Image Velocimetry (PIV) measurements in the centreplane. Simulated and measured jet trajectories are presented in Figure 7. The trajectory computed

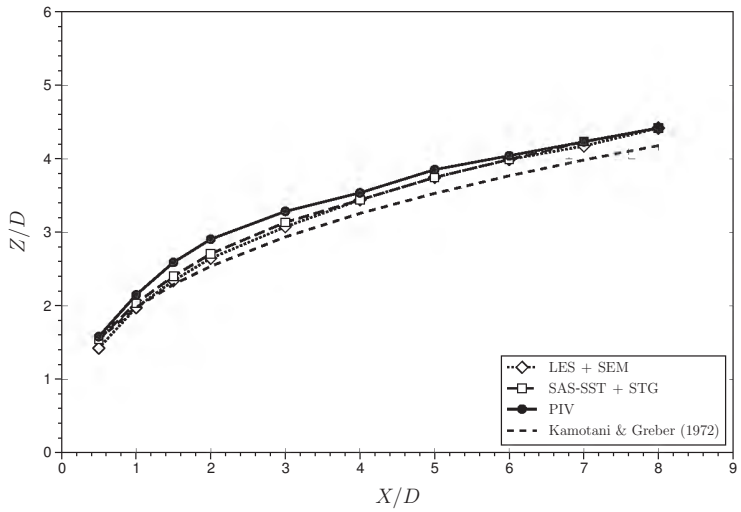

Figure 7: Jet trajectories based on local mean longitudinal velocity U maxima in the centreplane $Y/D = 0$.

with the correlation proposed by Kamotani & Greber Kamotani and Greber (1972) is also plotted for comparison. This correlation has been derived for a jet ejected with a uniform velocity profile. However, New *et al.* New et al. (2006) observed a higher penetration for jets ejected with a parabolic velocity profile compared to those with a uniform one. This can explain why the correlation predicts a slightly lower jet trajectory. Jet trajectory is well predicted by both LES + SEM and SAS-SST + STG calculations especially in the far field. It is worth noting that both approaches provide almost identical results regarding the jet trajectory. The main discrepancy between simula-

tions and measurements lies in the initial underestimation of jet lift-off by the calculations revealing a premature jet bending. As a result, simulated jet trajectories are located slightly below the experimental one. However, as X/D increases, simulations get in better agreement with the measurements.

4.3. Decay of velocity magnitude along jet trajectory

The decay of mean velocity magnitude $\|\vec{V}\|$ along the jet trajectory is plotted in Figure 8. This parameter provides a first order approximation of

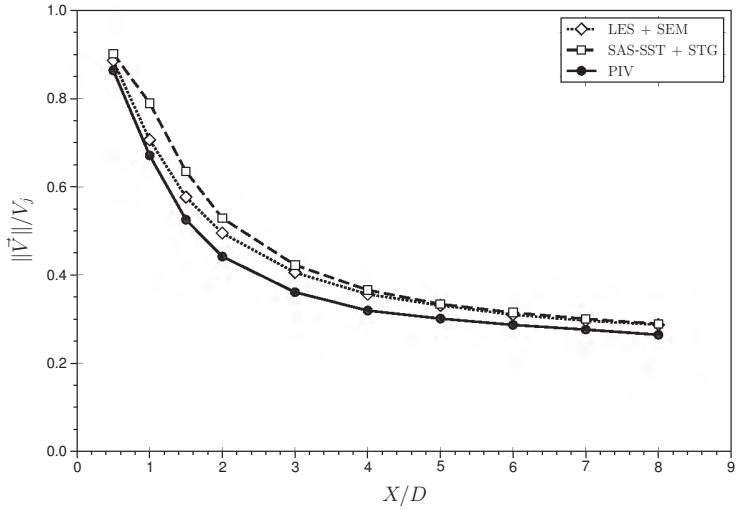

Figure 8: Decay of mean velocity magnitude $\|\vec{V}\|$ along jet trajectory.

the mixing process occurring between the jet and the crossflow. It is a rough estimate of the rate at which jet core momentum diffuses towards the outer regions under the action of turbulent mixing. One can see a rapid and nearly linear decay of the mean velocity magnitude in the initial development of the jet (up to $X/D = 1.5$). Between $X/D = 0$ and $X/D = 1.5$, $\|\vec{V}\|$ drops down by almost 50% of its initial value V_j over a distance of $1.5D$. Between

$X/D = 1.5$ and $X/D = 4.0$, the decay rate decreases drastically. Beyond $X/D = 4.0$, the decay rate recovers a constant value which is significantly smaller than the initial one (there is a factor 24 between the two decay rates) and $\|\vec{V}\|$ slowly converges towards V_{cf} (i.e. $\|\vec{V}\|/V_j = 0.27$). It is assumed that the change of behaviour occurring around $X/D = 4.0$ is due to the fact that beyond $X/D = 4.0$ the jet is completely aligned with the crossflow. As can be seen on time-averaged vertical velocity W profiles presented in Figure 12, the vertical component of jet core velocity is negligible at $X/D = 4.0$. Regarding simulation results, it can be seen that, between the first two stations ($X/D = 0.5$ and 1), the LES + SEM is in good agreement with the experimental measurements while the SAS-SST + STG strongly underestimates $\|\vec{V}\|$ decay. Beyond $X/D = 1.0$, the slow down of $\|\vec{V}\|$ decay occurs too prematurely in the LES + SEM calculation compared to the measurements. On the contrary, $\|\vec{V}\|$ decay increases in the SAS-SST + STG simulation so that SAS-SST + STG results progressively catch-up with LES + SEM results. In the far field, both simulation approaches recover the correct asymptotic behaviour. Simulated $\|\vec{V}\|$ decay rates are in good agreement with the measurements although simulated $\|\vec{V}\|$ levels are slightly shifted towards higher values.

4.4. Mean velocity fields

Simulated time-averaged velocity fields have been compared to measured ones. It is worth noting that the estimation of measurement uncertainties in PIV is delicate. However, it is assumed that measurement uncertainties on the mean velocity are about 0.7 m/s in the wake region, 0.05 m/s in the farfield and 2.5 m/s in the jet at a distance of 85 mm above the pipe outlet in

the present case. Figure 9 presents the contour plots of the mean longitudinal velocity U in the centreplane $Y/D = 0$. All physical features of the flow such as the recirculation zone on the windward side, the wake region on the lee side and the velocity overshoot in the jet core are captured by the simulations. Regarding the wake region, only the SAS-SST + STG captures the small bubble of higher U velocity located close to the wall around $X/D \approx 1.5$. This is likely due to the RANS fallback capability of the model in the vicinity of the wall where the grid is not fine enough to properly resolve the flow in LES. Both simulation approaches slightly underestimate the extent of the wake region. This is most likely due to the premature jet bending over as seen in Figure 7 which leads to a reduced blockage effect of the jet onto the crossflow. In addition, one can see that the velocity overshoot within jet core is overestimated and its decay is underestimated which is coherent with the observations made previously on $\|\vec{V}\|$ decay plots.

Figure 10 presents time-averaged profiles of the longitudinal velocity U normalized by crossflow velocity V_{cf} in the centreplane for X/D up to 4.0. These plots provide more quantitative information and complement the qualitative analysis carried out on contour plots. Several areas can be seen on these plots. For the highest Z/D values, one can notice a region where crossflow is unaffected by the presence of the jet so that $U/V_{cf} = 1.0$. As Z/D decreases, the profiles exhibit a strong velocity gradient materializing the upstream shear layer which makes the link between the freestream region and the jet core. For the first profiles located at $X/D = 0.5$ and 1.0, a small velocity deficit ($U/V_{cf} < 1.0$) can be noticed at the junction between the freestream and the upstream shear layer (around $Z/D = 2.2$ at $X/D = 0.5$

and $Z/D = 3.0$ at $X/D = 1.0$). This small velocity deficit ($U/V_{cf} = 0.75$ at $X/D = 0.5$ and $U/V_{cf} = 0.9$ at $X/D = 1.0$) is due to the blockage effect induced by the jet onto the crossflow. Below the upstream shear layer, one can see the jet core region which is characterised by a velocity overshoot ($U/V_{cf} > 1.0$) whose intensity decreases as distance downstream increases due to the mixing process occuring between the jet and the crossflow. Below the jet core, the downstream shear layer is materialised by a second area exhibiting a strong velocity gradient. The downstream shear layer makes the link between the jet core and the wake region. The latter is characterised by a velocity deficit which is progressively recovered as distance downstream increases. Close to the wall, a small bump in the velocity profile can be seen for $X/D \geq 1.0$. This small bump is likely due to the transport of higher momentum fluid located away from the wall toward the centreplane by the counter-rotating vortices. As underlined previously, simulations globally capture the main features of the flow. However, it can be seen on simulated profiles that the velocity overshoot is overestimated and located closer to the wall in the calculations. As mentioned above, jet bending over occurs sooner in the calculations decreasing jet lift-off and leading to an anticipated reorientation of jet momentum along crossflow direction. In addition, the velocity gradient $\partial U/\partial z$ is overestimated in both upstream and downstream shear layers revealing shear layers of higher intensity in the simulations. The velocity deficit in the wake region is also slightly underestimated by both simulation approaches.

Figure 11 presents the contour plots of the mean vertical velocity W in the centreplane $Y/D = 0$. It can be seen on the plots that the vertical

momentum introduced by the jet is rapidly reoriented. Vertical velocity levels have already dropped down to negligible levels beyond $X/D = 4$. Below the jet core, a region of upward velocities in the wake can be seen on the three plots. This upward motion of the flow in the centreplane is induced by the counter-rotating vortices. There are two main differences between simulations and measurements on these plots. On the one hand, W maxima near the pipe outlet are slightly shifted downstream in both calculations while they are almost centered in the measurements. This is coherent with the premature jet bending over mentioned before. On the other hand, it can be seen that calculations overestimate the intensity of the upward motion highlighting that the counter-rotating vortices intensity is overestimated. As jet lift-off is closely linked to counter-rotating vortices in the far field, the overestimation of their intensity can explain why simulated jet trajectories catch-up with measurements in the far field while jet bending over is initially overestimated.

Figure 12 presents time-averaged profiles of the vertical velocity W normalized by crossflow velocity V_{cf} for X/D up to 4.0. Two peaks can be noticed on the profiles. The upper peak, which is present since $X/D = 0.5$, is due to the upward momentum introduced by the jet. As distance downstream increases, it is progressively shifted towards higher values of Z/D as jet penetrates further into the crossflow. Its intensity rapidly decreases as the jet becomes progressively aligned with the crossflow. The lower peak, which gradually appears as distance downstream increases, materializes the establishment of the counter-rotating vortex pair. As mentioned before, the counter-rotating vortices induce an upward motion of the flow in the centre-

plane. From $X/D = 2.0$, one can notice that the intensity of the upward flow motion slowly decreases while the peak widen. Regarding the calculations, one can see that the upper peak is correctly captured even though it is located at a slightly lower altitude compared to the measurements. In contrast, one can notice a premature appearance of the lower peak in simulated profiles. At first, its intensity is largely overestimated with respect to the measurements but as distance downstream increases simulations get in better agreement with the measurements.

All mean flow comparisons between simulations and measurements carried out so far have been restricted to the centerplane. In order to further validate computational results against measurements, it is therefore necessary to investigate how they compare outside the centreplane. Figure 13 presents contour plots of in-plane mean velocity magnitude $V_{yz} = \sqrt{V^2 + W^2}$ with vectors of in-plane mean velocity in three transverse planes located at $X/D = 1.0$, 2.0 and 3.0.

Cross sections analysis is only carried out up to $X/D = 3.0$ as flow is well established beyond this location and transversal velocities V and W levels are low for $X/D \geq 3.0$. The progressive establishment of the counter-rotating vortex pair as distance downstream increases is clearly seen on these plots. PIV measurements reveal some asymmetries in the development of the counter-rotating vortex pair which will also be seen on temperature measurements later. However, they tend to disappear as X/D increases. Regarding levels of in-plane mean velocity magnitude, it can be seen that LES + SEM and SAS-SST + STG approaches provide similar results as expected according to the analysis performed in the centreplane. Both simulations overes-

timate the intensity of the counter-rotating vortices which results in higher levels of in-plane mean velocity magnitude. As pointed out previously on time-averaged vertical velocity W profiles in the centreplane, the higher intensity of the counter-rotating vortices induces a stronger upward motion of the flow in the centreplane. Figure 13 also provides an insight on the mechanism causing the accelerated velocity recovery in the wake in the simulations. The counter-rotating vortices induce close to the wall an inward flow motion towards the centreplane that feeds wake region with higher momentum fluid. As counter-rotating vortices intensity is overestimated in the simulations, this effect is overestimated as well leading to an accelerated velocity recovery in the wake.

In conclusion, mean flow topology is well reproduced by the simulations. Both simulation approaches capture the physical features of the flow. Some small discrepancies can be noticed between the measurements and the simulations in the near field. However, the agreement with measurements is enhanced going downstream. Finally, it can be seen that both approaches provide very similar results regarding mean flow dynamics.

4.5. Reynolds stresses

To further investigate the accuracy of LES and SAS simulations, simulated Reynolds stresses have been compared to measured ones. Figure 14 presents the contour plots of the Reynolds normal stress $\overline{u'u'}$ in the centreplane. To a first order approximation, normal stress $\overline{u'u'}$ levels follow its production term which can be simplified as follows in the centreplane:

$$P_{\overline{u'u'}} = -2\rho\overline{u'u'}\frac{\partial U}{\partial x} - 2\rho\overline{u'w'}\frac{\partial U}{\partial z} \tag{1}$$

The first term on the right hand side of Eq. (1) has the opposite sign than $\partial U/\partial x$. It is negative within the upstream shear layer and positive within the downstream shear layer. Therefore, it acts as a sink term within the upstream shear layer and as a source term in the downstream shear layer. The evolution of the second term is not as straightforward. One can see on plots presented in Figure 10 that the velocity gradient $\partial U/\partial z$ is positive across the downstream shear layer and negative across the upstream one. As a consequence, the term $-2\rho\overline{u'w'}\partial U/\partial z$ always has the same sign than $\overline{u'w'}$ in the upstream shear layer and the opposite one in the downstream shear layer. Contours of the Reynolds shear stress $\overline{u'w'}$ in the centreplane are plotted in Figure 16. It can be noticed that $\overline{u'w'}$ changes sign in both shear layers depending on distance downstream. From Figure 16, it can be seen that in the early development of the jet, the term $-2\rho\overline{u'w'}\partial U/\partial z$ acts as a sink term within both shear layers. As distance downstream increases, $\overline{u'w'}$ changes sign in both shear layers and $-2\rho\overline{u'w'}\partial U/\partial z$ then acts as a source term. To summarize, the two leading terms in the production of $\overline{u'u'}$ compete within the downstream shear layer close to pipe outlet leading to a progressive increase in $\overline{u'u'}$ levels. As distance downstream increases, the second term switches from a sink term to a source term. At this point, both terms contribute to the production of $\overline{u'u'}$ within the downstream shear layer leading to high levels of $\overline{u'u'}$. Further away, levels of $\overline{u'u'}$ slowly vanish as velocity gradients within the shear layers weaken under the action of turbulent mixing. On the other hand, within the upstream shear layer, both terms act as sink terms in the early development of the upstream shear layer leading to low levels of $\overline{u'u'}$. As distance downstream increases, the second term in the production of $\overline{u'u'}$ becomes a source term

competing with the first one which still acts as a sink term. Therefore, only moderate levels of $\overline{u'u'}$ can be observed in the upstream shear layer due to the competition between the two terms and the fact that velocity gradient $\partial U/\partial z$ has already significantly decreased when this term switches to a source term. Regarding simulation results, it can be seen that the topology of the $\overline{u'u'}$ field is correctly reproduced. As can be seen in Figure 14, simulations exhibit slightly higher levels of $\overline{u'u'}$ within jet shear layers compared to PIV measurements. This is particularly perceptible within the jet upstream shear layer where measured $\overline{u'u'}$ levels are almost null. The LES approach presents a thicker area of high $\overline{u'u'}$ levels within the downstream shear layer. In addition, one can notice the presence of high levels of $\overline{u'u'}$ stress within the upstream shear layer close to the pipe outlet.

Figure 15 presents the contour plots of the Reynolds normal stress $\overline{w'w'}$ in the centreplane.

As mentioned before for $\overline{u'u'}$, the normal stress $\overline{w'w'}$ levels follow, to a first order approximation, its production term which can be simplified as follows in the centreplane:

$$P_{\overline{w'w'}} = -2\rho\overline{u'w'}\frac{\partial W}{\partial x} - 2\rho\overline{w'w'}\frac{\partial W}{\partial z} \tag{2}$$

One can see that the simplification of the production term of the normal stress $\overline{w'w'}$ is analogous to the one previously done for $\overline{u'u'}$. Starting with the second term on the right hand side of Eq. (2), it can be seen on profiles of mean vertical velocity W presented in Figure 12 that $\partial W/\partial z$ is positive across the downstream shear layer and negative across the upstream one. Therefore, the term $-2\rho\overline{w'w'}\partial W/\partial z$ acts as a sink term within the

downstream shear layer and as a source term within the upstream one. On the other hand, the velocity gradient $\partial W/\partial x$ is positive across the upstream shear layer and negative across the downstream one. As a consequence, the term $-2\rho\overline{u'w'}\partial W/\partial x$ has the same sign than $\overline{u'w'}$ within the downstream shear layer and the opposite one in the upstream shear layer. From $\overline{u'w'}$ contour plots presented in Figure 16, it appears that the term $-2\rho\overline{u'w'}\partial W/\partial x$ acts in both shear layers as a source term in the early development of the jet then switches to a sink term. As a result, both terms act as source terms within the upstream shear layer as the jet leaves the pipe leading to an increase in $\overline{w'w'}$ levels. Further away, the term $-2\rho\overline{u'w'}\partial W/\partial x$ becomes a sink term and starts to compete with the other term in the production of $\overline{w'w'}$. Within the downstream shear layer, both terms compete in the early beginning of jet development leading to moderate levels of $\overline{w'w'}$. Further downstream, both terms become sink terms and levels of $\overline{w'w'}$ decrease. Regarding simulation results, it can be noticed that normal stress $\overline{w'w'}$ levels in the centreplane are slightly underestimated by the SAS-SST + STG approach within the upstream shear layer. The LES + SEM approach provides results in better agreement with PIV measurements even though the area of high fluctuations is slightly thicker. Although small discrepancies can be noticed, LES and SAS approaches give a fair prediction of $\overline{w'w'}$ levels in the centreplane.

Figure 16 presents the turbulent shear stress $\overline{u'w'}$ field in the centreplane.

It can be seen that the field topology is well captured by the simulations. However, absolute levels are overestimated. This behaviour was expected

as it has been noticed on mean velocity profiles that shear layers are more intense in the calculations. The complete analysis of the Reynolds shear stress $\overline{u'w'}$ field will not be performed in the present paper as it is not as straightforward as the ones carried out for the normal stresses.

4.6. Turbulent kinetic energy

Figure 17 presents the contour plots of turbulent kinetic energy k in the centreplane.

As k is equal to half the trace of the Reynolds stress tensor, the analysis is closely linked to the one previously done on the normal stresses. As expected, high levels of turbulent kinetic energy are found within shear layers regions. Further downstream, levels of k drop rapidly. Regarding simulated contours, it can be noticed that levels of turbulent kinetic energy within shear layers are overestimated by both simulation approaches. The LES approach predicts higher levels of k than the SAS-SST approach. This is especially true within the downstream shear layer.

4.7. Thermal aspects

Turbulent mixing between the jet and the crossflow is of primary interest for helicopters applications. Forecasting the thermal footprint of engines' exhaust gases onto the fuselage does not only require a good prediction of plumes trajectories. Contour plots of normalized mean static temperature fields $\theta = (T - T_{cf})/(T_j - T_{cf})$ in three transverse planes are presented in Figure 18. Simulation results are compared to thermocouple measurements. The measurement uncertainty on temperature measurements is about $\pm 1\,\mathrm{K}$. The thermal field topology of the jet is well captured by the simulations.

Slightly higher temperature levels can be observed in the simulations in the considered transverse planes. This observation underlines that the turbulent mixing of the jet and the crossflow is slightly underestimated in the simulations. However, discrepancies between simulations and measurements tend to decrease as distance downstream X/D increases. It is assumed that the higher temperature levels in the SAS calculation are caused by the delay observed in the simulation to switch from its RANS solving mode to its scale resolving mode.

Figure 19 shows the time-averaged temperature profiles in the centreplane at the locations of the three transverse planes introduced before (i.e. $X/D = 0.5$, 1.5 and 3.0). These profiles allow to quantify the discrepancies between simulations and measurements. One can see that the temperature peak intensity is correctly predicted by both simulation approaches although it is very slightly overestimated by the SAS-SST approach at $X/D = 0.5$. Regarding its location, the LES approach tends to underestimate its altitude at the first two stations ($X/D = 0.5$ and 1.5) but catch-up with measurements at $X/D = 3.0$. Small discrepancies between measured and simulated profiles can be observed in the vicinity of the wall, the latter exhibiting slightly lower temperature levels. It is assumed that these differences are consequences of the overestimation of the counter-rotating vortices intensity inducing a higher entrainment of cold flow toward the centreplane close to the wall.

In order to further investigate the turbulent mixing process occurring in the present jet in crossflow configuration, it is interesting to examine the turbulent heat flux along each direction. Therefore, the three components of the time-resolved turbulent heat flux vector (i.e. $\overline{u'T'}$, $\overline{v'T'}$ and $\overline{w'T'}$)

obtained with the SAS-SST + STG simulation are plotted in the same three transverse planes in Figure 20.

It can be seen that the lateral component of the turbulent heat flux $\overline{v'T'}$, which is linked to the lateral diffusion of the jet, exhibits levels of about half the other two components. Although the lateral turbulent diffusion cannot be neglected, as it remains about the same order of magnitude than the longitudinal and vertical components, it is not the dominant mixing process in the present jet in crossflow configuration. In contrast, the highest levels are encountered for the vertical component of the turbulent heat flux $\overline{w'T'}$. Putting aside the cross section located at $X/D = 0.5$, the main contribution to the total turbulent heat flux is, as could be expected, brought by the component $\overline{w'T'}$ within the jet upstream shear layer. This underlines that shear-layer roll-up, especially within the upstream mixing layer, plays a significant role in the jet in crossflow turbulent mixing process. Therefore, it is assumed that the good resolution of the Kelvin-Helmholtz instability onset as well as the resulting shear-layer roll-up is essential to the correct simulation of jets in crossflow turbulent mixing.

It is worth noting that both approaches used in this study directly resolve the turbulent heat flux unlike steady-state RANS calculations which require a closure for the turbulent heat flux. As dynamics and thermal fields obtained from present simulations have been validated against measurements, resolved turbulent heat flux can therefore be used to evaluate RANS closures for the turbulent heat flux. Such analysis has been carried out on turbulent scalar flux models by Ling *et al.* Ling et al. (2016) and Ryan *et al.* Ryan et al. (2017) using LES simulations of an incompressible skewed jet in crossflow at

a blowing ratio of unity. Stratton & Shih Stratton and Shih (2019) also used LES simulations to investigate the suitability of the Gradient-Diffusion Hypothesis (GDH) closure for a 35° inclined jet at different blowing ratios and density ratios. All studies have pointed out that GDH modelling failed to reproduce the turbulent heat flux in the case of jets in crossflow. They also evidenced that the turbulent Prandtl number Pr_t which is commonly considered constant strongly varies spatially. Nevertheless, in all three studies, the jet remained attached or close to the wall due to the low values of the considered blowing ratios. Therefore, present work aims at increasing the scope of validity of these results to a jet in crossflow with a higher momentum flux ratio and a strong temperature gradient. In the present paper, the analysis will be restricted to the investigation of the GDH model which is the most widely used turbulent heat flux modelling as mentioned previously. The latter expresses the turbulent heat flux as the product of a turbulent diffusivity with the temperature gradient following a Fourier's law.

$$\overline{u_i'T'}_{GDH} = -\alpha_t \frac{\partial T}{\partial x_i} \tag{3}$$

where α_t is the turbulent diffusivity. The turbulent diffusivity is usually computed through the Reynolds analogy using a constant turbulent Prandtl number Pr_t as:

$$\alpha_t = \frac{\nu_t}{Pr_t} \tag{4}$$

where ν_t is the turbulent viscosity. From Eq. 3, it is possible to compute a value of the turbulent diffusivity by direction ($\alpha_{t,x}$, $\alpha_{t,y}$ and $\alpha_{t,z}$) using the time-resolved turbulent heat fluxes $\overline{u_i'T'}$ and their associated temperature gradients $\partial T/\partial x_i$ extracted from the scale-resolving calculations. The

analysis has been undertaken for the SAS-SST calculation and results are presented in Figure 21.

Directional turbulent diffusivity has been set to zero outside jet envelope where $\theta < 0.01$. One can see from Figure 21 that directionals values of α_t at a given location strongly vary depending on the direction considered highlighting the strong anisotropy of the turbulent diffusivity field. These results are in good agreement with previous studies Ling et al. (2016); Ryan et al. (2017); Stratton and Shih (2019) and point out that isotropic eddy viscosity models coupled to a GDH closure for the turbulent heat flux cannot correctly predict turbulent mixing of such flow.

As briefly mentioned before, another assumption commonly made in RANS calculations is to consider that Pr_t is constant with a value of about $0.85 - 0.9$. These values are derived from boundary layer flows for which the turbulent Prandtl number exhibits a plateau of $Pr_t \approx 0.85 - 0.9$. However, even in a boundary layer, Pr_t is not constant and different values have been proposed for jet and wake flows. Having access to time-resolved turbulent fluxes allows therefore to assess the suitability of this hypothesis for the present flow configuration using Eq. 3 and 4. As mentioned earlier, when operating in their scale resolving mode, scale-resolving simulations directly resolve large scale turbulence structures instead of modelling their influence onto the mean flow through the computation of an eddy viscosity. Therefore, it is necessary to compute an equivalent eddy viscosity from time-averaged variables in order to derive a turbulent Prandtl number. However, unlike the turbulent diffusivity which is a vector, the eddy viscosity is a tensor. As a result, deriving a directional eddy viscosity from time-averaged variables

is not as straightforward as for the turbulent diffusivity. A more relevant approach is thus to compute an equivalent isotropic eddy viscosity. Such an isotropic eddy viscosity $\nu_{t,iso}$ can be computed with the following relation as proposed by Stratton & Shih Stratton and Shih (2019):

$$\nu_{t,iso} = \frac{-\overline{u_i' u_j'}\left(S_{ij} - \frac{1}{3}\frac{\partial U_k}{\partial x_k}\delta_{ij}\right) + \frac{2}{3}k\delta_{ij}\left(S_{ij} - \frac{1}{3}\frac{\partial U_k}{\partial x_k}\delta_{ij}\right)}{2\left(S_{lm} - \frac{1}{3}\frac{\partial U_k}{\partial x_k}\delta_{lm}\right)\left(S_{lm} - \frac{1}{3}\frac{\partial U_k}{\partial x_k}\delta_{lm}\right)} \tag{5}$$

where S_{ij} is the mean rate of strain tensor. Ling *et al.* Ling et al. (2016) and Ryan *et al.* Ryan et al. (2017) used the incompressible form of Eq. 5 in their studies. To compute the equivalent isotropic eddy viscosity, a weighted average is performed over the eddy viscosity yielded by each component of the resolved Reynolds stress tensor using Boussinesq's hypothesis. The weighting is based on the components of the strain rate tensor. Similarly, an equivalent isotropic turbulent diffusivity can be computed through a weighted average of the resolved turbulent diffusivity in each direction as in Eq. 6. The weighting is based here on the temperature gradients in the corresponding direction.

$$\alpha_{t,iso} = \frac{-\overline{u_i' T'}\frac{\partial T}{\partial x_i}}{\overline{\frac{\partial T}{\partial x_j}}\overline{\frac{\partial T}{\partial x_j}}} \tag{6}$$

Figure 22 presents the isotropic eddy viscosity $\nu_{t,iso}$, turbulent diffusivity $\alpha_{t,iso}$ and turbulent Prandtl number $Pr_{t,iso}$ fields computed from the time-averaged variables extracted from the SAS-SST calculation in three transverse planes (X/D = 0.5, 1.5 and 3.0). As for the directional turbulent diffusivity plots, isotropic $\alpha_{t,iso}$ and $Pr_{t,iso}$ have been set to zero outside jet envelope where $\theta < 0.01$. As expected, high values of $\nu_{t,iso}$ are found within

shear layers and jet wake where turbulence levels are strong. As such, $\nu_{t,iso}$ does not have much interest in itself if not compared to a field obtained from a RANS calculation. Turbulent Prandtl number value is strongly varying spatially for the present flow configuration highlighting that the assumption of constant Pr_t is not relevant to correctly reproduce the turbulent heat flux in the case of jets in crossflow. Pr_t exhibits values around $0.6 - 0.7$ in the upstream mixing layer and mainly smaller than 0.6 in the wake region which are lower than commonly used values of $0.85 - 0.9$. Considering that the GDH closure would be well suited for the modelling of the turbulent heat flux in the case of jets in crossflow, which is not the case as shown before, the hypothesis $Pr_t \approx 0.85 - 0.9$ would result in an underestimation of the turbulent heat flux.

5. Influence of pipe inflow conditions

As mentioned previously, the present study has also evidenced that the boundary conditions imposed at pipe inlet have a significant influence on simulation accuracy. First of all, it is worth recalling that the SAS approach relies on inherent flow instabilities to switch from its RANS mode to its scale-resolving mode. In the present cas, the prescription of fully developed pipe inflow conditions extracted from a precursor steady-state RANS calculation leads to a stable flow inside the pipe which can be solved in RANS. As a result, a delayed transition from RANS to LES is observed in the SAS approach. This delayed RANS to LES transition is a well-known defect of hybrid RANS/LES approaches. It is sometimes referred to as the "grey area" issue Gand (2016). To overcome this issue in the present case, a solution

consists in adding time and space varying perturbations to the velocity profiles at the pipe inlet. This approach is referred to as synthetic turbulence injection. This strategy has been successfully applied by Gand Gand (2016) for the simulations of free jets. He performed Zonal Detached Eddy Simulations (ZDES) of free jets and observed an accelerated transition from RANS to scale resolving mode of the models when synthetic turbulence is injected within the jet upstream its ejection location.

5.1. Influence on the flow field

Regarding the SAS-SST calculations, the injection of synthetic turbulence at the pipe inlet leads to a decrease in the turbulent to molecular viscosity ratio as shown in Figure 23. This decrease of ν_t/ν is particularly pronounced within the core of the pipe. As a consequence, the addition of synthetic turbulence to the pipe inflow accelerates the RANS to LES transition of the SAS-SST model. A direct consequence of this decrease in viscosity ratio is the earlier occurrence of shear layer roll-up highlighting that the model starts to resolve flow turbulence sooner. To illustrate this remark, Figure 24 presents two snapshots of the instantaneous normalized temperature $\theta = (T - T_{cf})/(T_j - T_{cf})$ in the centreplane $Y/D = 0$. These snapshots are extracted from two SAS-SST calculations performed with and without synthetic turbulence injection at the pipe inlet. As mentioned previously, one can see that the injection of synthetic turbulence at the pipe inlet results in an earlier occurence of shear-layer roll-up. Within the upstream shear-layer, one can observe that roll-up is initiated at an altitude of about $0.4D$ when synthetic turbulence is injected at the pipe inlet while it is delayed to about $0.6D$ without synthetic turbulence.

Regarding mean flow features, the influence of synthetic turbulence injection at the pipe inlet on the jet trajectory and mean temperature field is investigated for the two turbulence modelling approaches studied (i.e. LES and SAS-SST). Jet trajectories simulated with and without synthetic turbulence injection are presented in Figure 25.

Plots presented in Figure 25 reveal that synthetic turbulence injection has only a minor influence on the jet trajectory predicted by the SAS-SST approach. In contrast, it strongly influences the jet trajectory predicted by the LES approach. Although the LES calculation carried out without addition of synthetic turbulence to the pipe inflow gives a good prediction of jet trajectory up to $X/D = 2.0$, it overestimates the jet lift-off further downstream. This observation is likely due to the underestimation of turbulence levels within the jet without synthetic turbulence injection at the pipe inlet.

Figure 26 presents the mean normalized temperature fields in the transverse plane $X/D = 3.0$ measured and simulated with and without synthetic turbulence injection at the pipe inlet.

It can be seen that the addition of synthetic turbulence to the pipe inflow leads to a better prediction of the mean temperature field. A decrease in simulated temperature levels within the jet plume is observed resulting in a better agreement with the experimental data. Regarding the SAS-SST approach, the better forecast of the turbulent mixing is likely due to the accelerated RANS to LES transition when synthetic turbulence is injected at the pipe inlet. Regarding the LES approach, the better prediction of the turbulent mixing is likely due the better prediction of turbulence levels within the jet when synthetic turbulence is injected at the pipe inlet as observed for

the jet trajectory.

6. Conclusions

In the present paper, a high-temperature turbulent jet in a cold crossflow is investigated with the help of two scale resolving simulation approaches (SAS-SST and LES). The present work has highlighted the importance of synthetic turbulence injection at pipe inlet to obtain a fair prediction of both flow dynamics and temperature field. When synthetic turbulence is injected at the pipe inlet, it has been shown that the mean flow topology is well reproduced by the simulations. Both simulation approaches capture the physical features of the flow. Small discrepancies have been noticed between measurements and simulations in the near field such as the overestimation of counter-rotating vortices intensity and the premature jet bending exhibited by the calculations. However, the agreement with measurements is enhanced as distance downstream increases. Results have also pointed out that both approaches provide very similar results regarding mean flow dynamics. Comparisons between simulations and measurements have also been undertaken for the turbulent quantities. The analysis has shown that both SAS-SST + STG and LES + SEM approaches provide a fair prediction of the Reynolds stresses in the centreplane. Turbulent kinetic energy levels are also well reproduced by the simulations even though the LES + SEM approach predicted slightly higher levels within jet shear layers. Thermal aspects of the flow have then been investigated by comparing measured and simulated mean temperature fields in several transverse planes. Simulated mean temperature levels within the plume were shown to be in good agreement with

experimental data highlighting that the simulations correctly reproduce the turbulent mixing between the jet and the crossflow. Finally, the analysis of resolved turbulent heat fluxes have revealed that the gradient diffusion hypothesis involving a constant Prandtl number which is classically used in steady-state RANS calculations is unappropriate to model the turbulent heat flux for this kind of flow. The turbulent diffusivity has been shown to be strongly anisotropic and the turbulent Prandtl number which is commonly considered constant with a value of 0.85 - 0.9 strongly varies spatially and exhibits smaller values within the wake region and jet shear-layers.

References

R. J. Margason, Fifty years of jet in cross flow research, in: AGARD-CP-534, Computational and Experimental Assessment of Jets in Cross Flow, 1993, pp. 1–1 to 1–41.

K. Mahesh, The interaction of jets with crossflow, Annual review of fluid mechanics 45 (2013) 379–407.

A. R. Karagozian, The jet in crossflow, Physics of Fluids 26 (2014) 1–47.

O. G. Sutton, A theory of eddy diffusion in the atmosphere, Proceedings of the royal society of London. Series A, Containing papers of a mathematical and physical character 135 (1932) 143–165.

C. Bosanquet, J. Pearson, The spread of smoke and gases from chimneys, Transactions of the Faraday Society 32 (1936) 1249–1263.

A. W. Carter, Effects of jet-exhaust location on the longitudinal aerodynamic characteristics of a jet V/STOL model, volume 5333, National Aeronautics and Space Administration, 1969.

G. Gentry Jr, R. Margason, Aerodynamic characteristics of a five jet VTOL configuration in the transition speed range, Technical Note NASA TN D-4812, NASA, 1968.

C. Hale, M. W. Plesniak, S. Ramadhyani, Film cooling effectiveness for short film cooling holes fed by a narrow plenum, J. Turbomach. 122 (2000) 553–557.

V. L. Eriksen, R. J. Goldstein, Heat transfer and film cooling following normal injection through a round hole, Journal of Engineering for Power 96 (1974) 329–334.

G. Arroyo-Callejo, E. Laroche, P. Millan, F. Leglaye, F. Chedevergne, Numerical investigation of compound angle effusion cooling using differential reynolds stress model and zonal detached eddy simulation approaches, Journal of Turbomachinery 138 (2016).

E. Ivanova, M. Di Domenico, B. Noll, M. Aigner, Unsteady simulations of flow field and scalar mixing in transverse jets, in: ASME Turbo Expo 2009: Power for Land, Sea, and Air, American Society of Mechanical Engineers, 2009, pp. 101–110.

H. Bézard, D. Donjat, P. Viguier, J. C. Jouhaud, S. Bocquet, Projet ASTHER - Analyse et Simulation des jets débouchants et de leur impact THERmique, Technical Note 2/15118 DMAE, ONERA, 2012.

F. C. C. Galeazzo, G. Donnert, C. Cárdenas, J. Sedlmaier, P. Habisreuther, N. Zarzalis, C. Beck, W. Krebs, Computational modeling of turbulent mixing in a jet in crossflow, International journal of heat and fluid flow 41 (2013) 55–65.

J. Prause, Y. Emmi, B. Noll, M. Aigner, LES/RANS modeling of turbulent mixing in a jet in crossflow at low velocity ratios, in: 54th AIAA Aerospace Sciences Meeting, 2016, p. 0609.

D. Rusch, L. Blum, A. Moser, T. Rösgen, Turbulence model validation for fire simulation by CFD and experimental investigation of a hot jet in crossflow, Fire Safety Journal 43 (2008) 429–441.

L. L. Yuan, R. L. Street, J. H. Ferziger, Large-eddy simulations of a round jet in crossflow, Journal of Fluid Mechanics 379 (1999) 71–104.

L. Zhang, V. Yang, Flow dynamics and mixing of a transverse jet in crossflow — Part I: Steady crossflow, Journal of Engineering for Gas Turbines and Power 139 (2017a) 082601.

L. Zhang, V. Yang, Flow dynamics and mixing of a transverse jet in crossflow — Part II: Oscillating crossflow, Journal of Engineering for Gas Turbines and Power 139 (2017b) 082602.

J. A. Denev, J. Fröhlich, H. Bockhorn, Large eddy simulation of a swirling transverse jet into a crossflow with investigation of scalar transport, Physics of Fluids 21 (2009) 015101.

J. C. Jouhaud, L. Y. M. Gicquel, B. Enaux, M. J. Esteve, Large-eddy-simulation modeling for aerothermal predictions behind a jet in crossflow, AIAA journal 45 (2007) 2438–2447.

B. M. Duda, M. J. Esteve, S. Deck, F. R. Menter, T. Hansen, H. Bézard, Numerical investigations on a hot jet in cross flow using scale-resolving simulations, in: TSFP DIGITAL LIBRARY ONLINE, Begel House Inc., 2011.

B. M. Duda, Etude et analyse numérique d'un jet chaud débouchant dans un écoulement transverse en utilisant des simulations aux échelles résolues, Ph.D. thesis, Toulouse, ISAE, 2012.

B. M. Duda, F. R. Menter, T. Hansen, M. J. Estève, S. Deck, H. Bézard, Aerothermal prediction of multiple hot jets in crossflow for aircraft applications, AIAA journal 52 (2014) 1035–1046.

D. Donjat, R. Paysant, E. Laroche, F. Micheli, L. Lanzillotta, P. Reulet, J. M. Deluc, P. Buet, An experimental analysis of a high temperature jet in crossflow, (Submitted to Experiments in Fluids) (2021).

F. R. Menter, Best Practice: Scale-Resolving Simulations in ANSYS CFD, ANSYS Germany GmbH Version 2.0 (2015).

J. P. Van Doormaal, G. D. Raithby, Enhancements of the simple method for predicting incompressible fluid flows, Numerical heat transfer 7 (1984) 147–163.

A. Refloch, B. Courbet, A. Murrone, P. Villedieu, C. Laurent, P. Gilbank,

J. Troyes, L. Tessé, G. Chaineray, J.-B. Dargaud, E. Quémerais, F. Vuillot, CEDRE Software, Aerospace Lab Journal 2 (2011) AL02–11.

F. Haider, B. Courbet, J.-P. Croisille, A high-order interpolation for the finite volume method: The Coupled Least Squares reconstruction, Computers & Fluids 176 (2018) 20–39.

F. R. Menter, Y. Egorov, The scale-adaptive simulation method for unsteady turbulent flow predictions. part 1: theory and model description, Flow, Turbulence and Combustion 85 (2010) 113–138.

P. Sagaut, S. Deck, M. Terracol, Multiscale and multiresolution approaches in turbulence: LES, DES and hybrid RANS/LES methods: applications and guidelines, World Scientific, 2013.

N. Jarrin, S. Benhamadouche, D. Laurence, R. Prosser, A synthetic-eddy-method for generating inflow conditions for large-eddy simulations, International Journal of Heat and Fluid Flow 27 (2006) 585–593.

N. Jarrin, Synthetic inflow boundary conditions for the numerical simulation of turbulence, Ph.D. thesis, university of Manchester, 2008.

N. Jarrin, R. Prosser, J.-C. Uribe, S. Benhamadouche, D. Laurence, Reconstruction of turbulent fluctuations for hybrid RANS/LES simulations using a Synthetic-Eddy Method, International Journal of Heat and Fluid Flow 30 (2009) 435–442.

M. L. Shur, P. R. Spalart, M. K. Strelets, A. K. Travin, Synthetic turbulence generators for RANS-LES interfaces in zonal simulations of aerodynamic

and aeroacoustic problems, Flow, turbulence and combustion 93 (2014) 63–92.

Y. Kamotani, I. Greber, Experiments on a turbulent jet in a cross flow, AIAA journal 10 (1972) 1425–1429.

T. New, T. Lim, S. Luo, Effects of jet velocity profiles on a round jet in cross-flow, Experiments in Fluids 40 (2006) 859–875.

J. Ling, K. J. Ryan, J. Bodart, J. K. Eaton, Analysis of turbulent scalar flux models for a discrete hole film cooling flow, Journal of Turbomachinery 138 (2016).

K. J. Ryan, J. Bodart, M. Folkersma, C. J. Elkins, J. K. Eaton, Turbulent scalar mixing in a skewed jet in crossflow: experiments and modeling, Flow, Turbulence and Combustion 98 (2017) 781–801.

Z. T. Stratton, T. I. Shih, Identifying weaknesses in eddy-viscosity models for predicting film cooling via large-eddy simulations, Journal of Propulsion and Power 35 (2019) 583–594.

F. Gand, Investigation of turbulence development in incompressible jets with zonal detached eddy simulation (ZDES) and synthetic turbulent inflow, International Journal of Heat and Fluid Flow 61 (2016) 425–437.

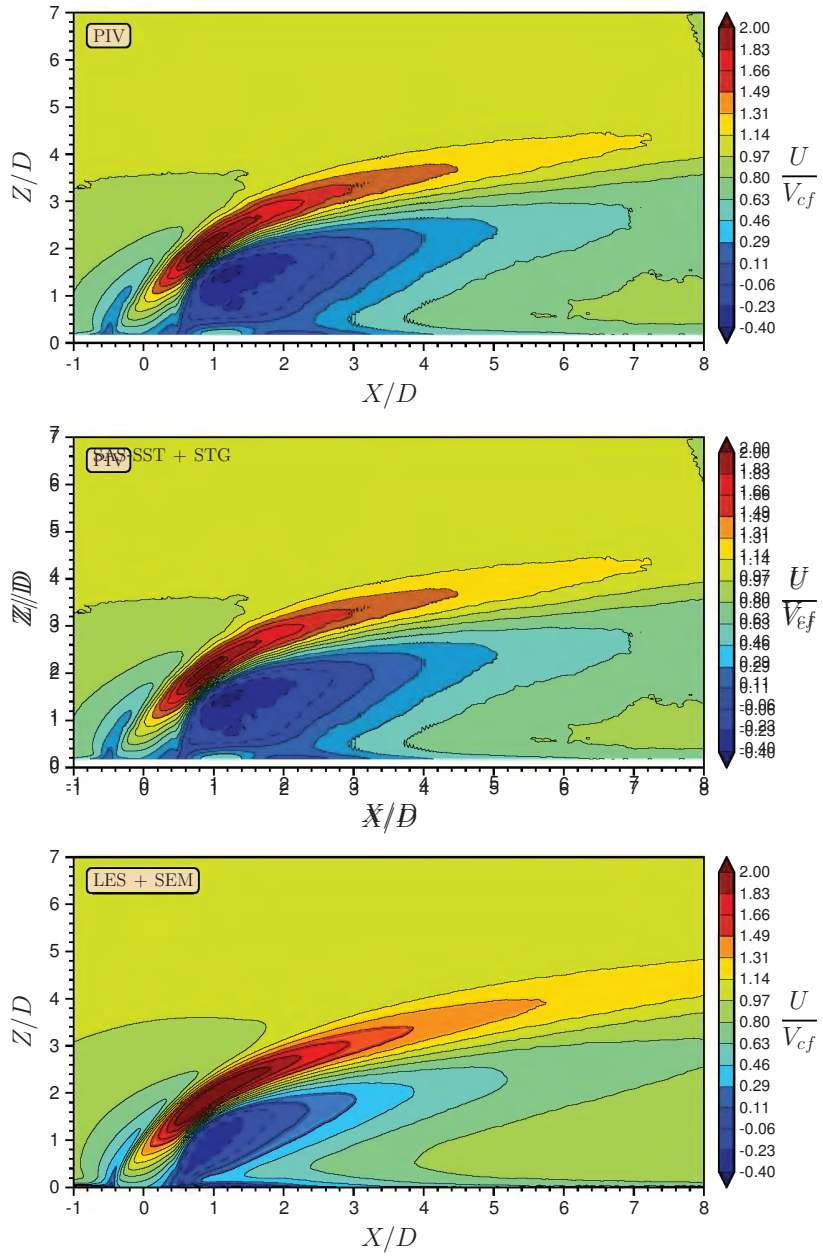

Figure 9: Mean longitudinal velocity U field in the centreplane $Y/D = 0$ normalized by crossflow velocity V_{cf}. From top to bottom: PIV measurements, SAS-SST + STG and LES + SEM.

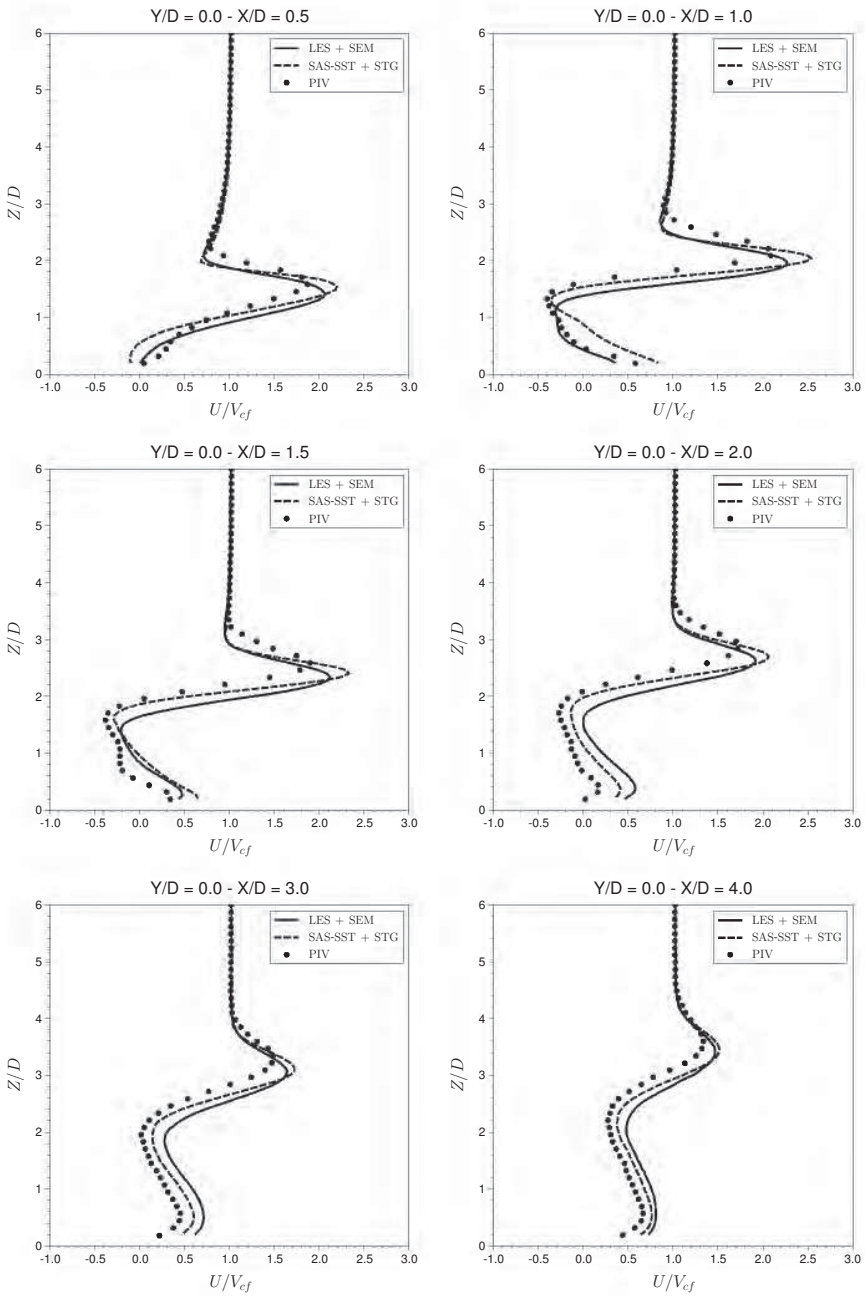

Figure 10: Time-averaged longitudinal velocity U profiles in the centreplane $Y/D = 0$ normalized by crossflow velocity V_{cf}.

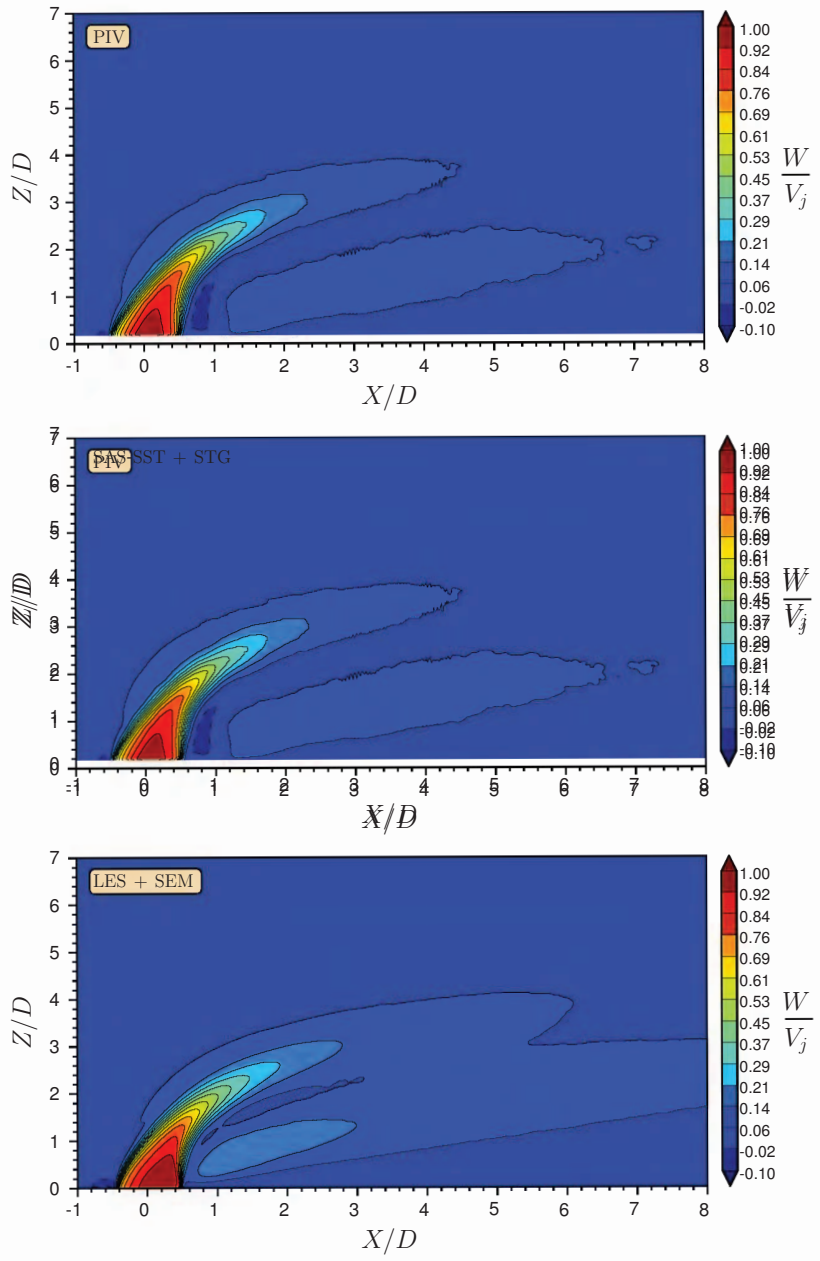

Figure 11: Mean vertical velocity W field in the centreplane $Y/D = 0$ normalized by jet velocity V_j. From top to bottom: PIV measurements, SAS-SST + STG and LES + SEM.

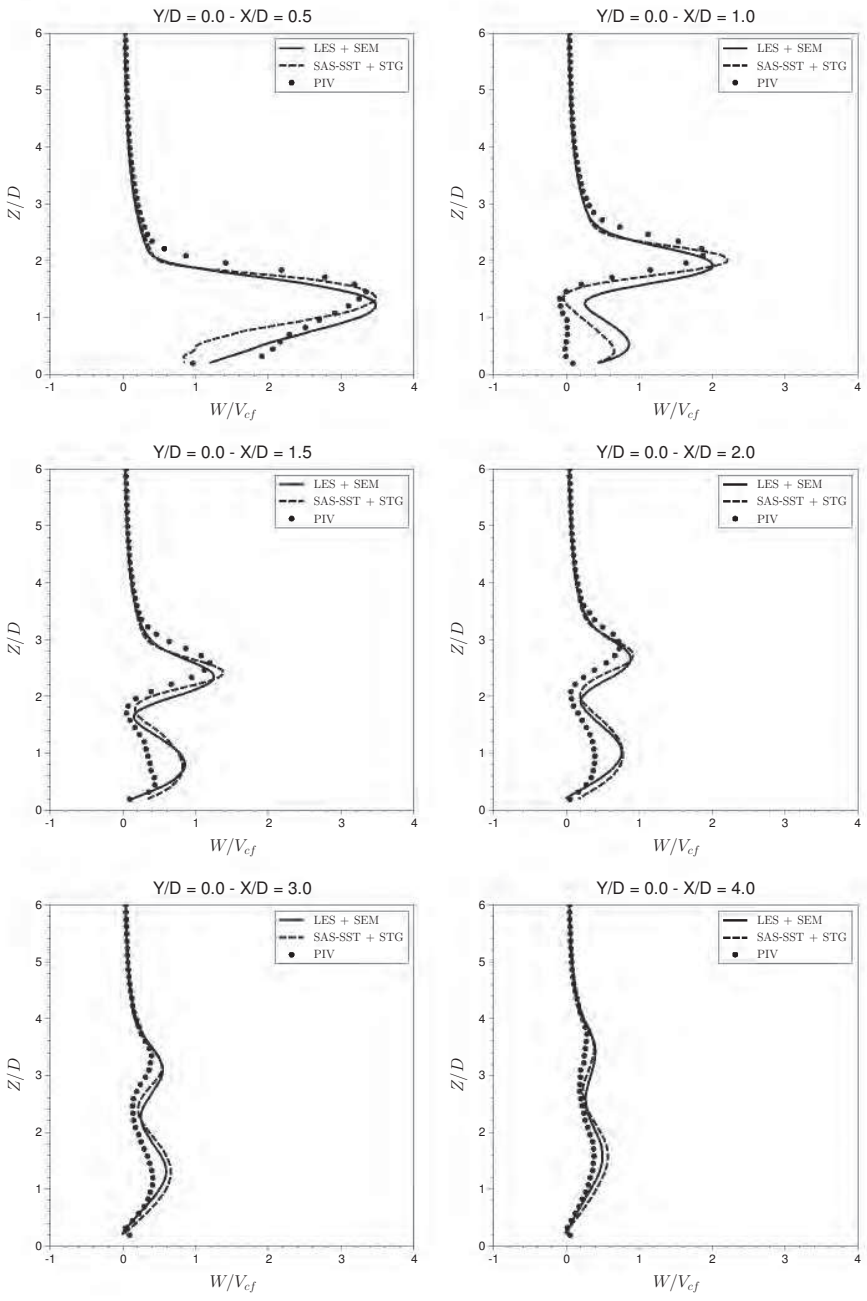

Figure 12: Time-averaged vertical velocity W profiles in the centreplane $Y/D = 0$ normalized by crossflow velocity V_{cf}.

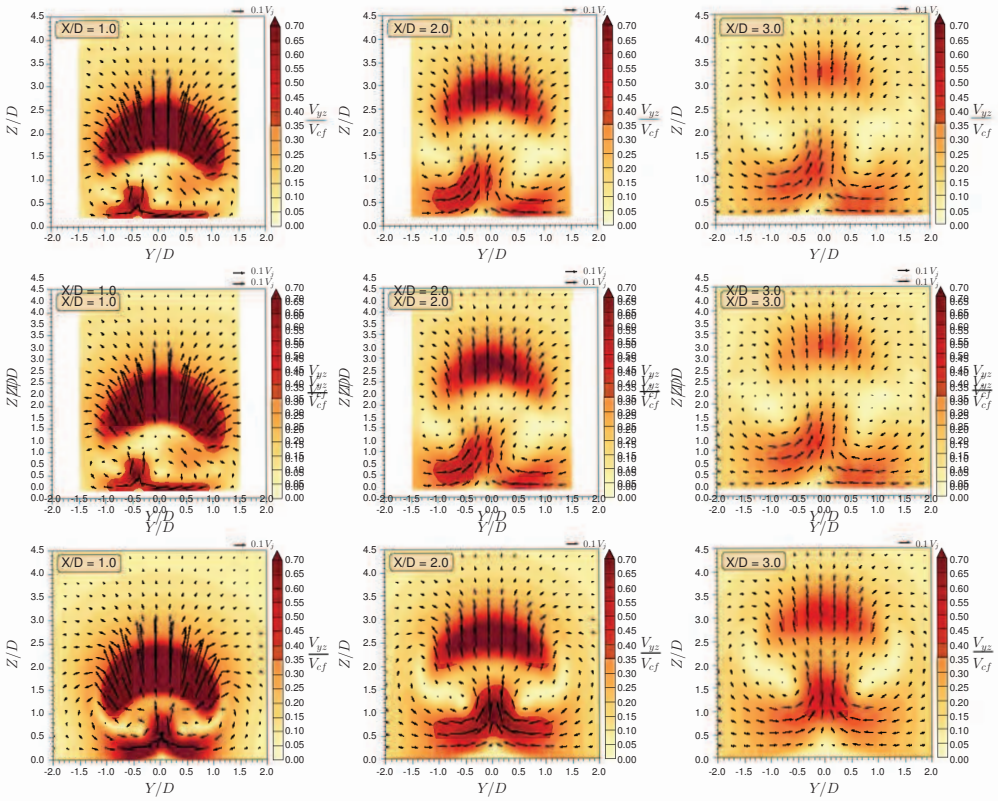

Figure 13: Contour plots of in-plane mean velocity magnitude $V_{yz} = \sqrt{V^2 + W^2}$ with vectors of in-plane mean velocity in three transverse planes (from left to right: $X/D = 1.0$, 2.0 and 3.0). From top to bottom: PIV measurements, SAS-SST + STG and LES + SEM.

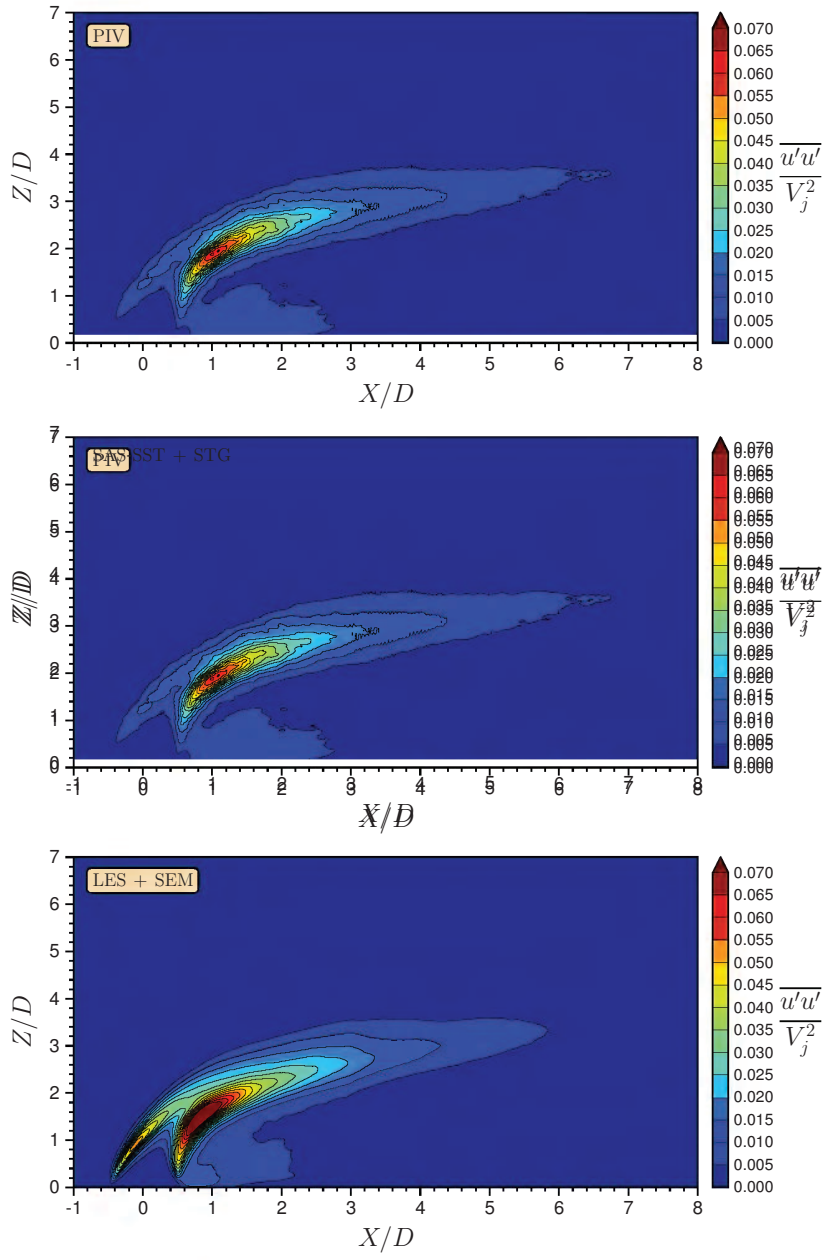

Figure 14: Reynolds normal stress $\overline{u'u'}$ field in the centreplane $Y/D = 0$ normalized by squared jet velocity V_j^2. From top to bottom: PIV measurements, SAS-SST + STG and LES + SEM.

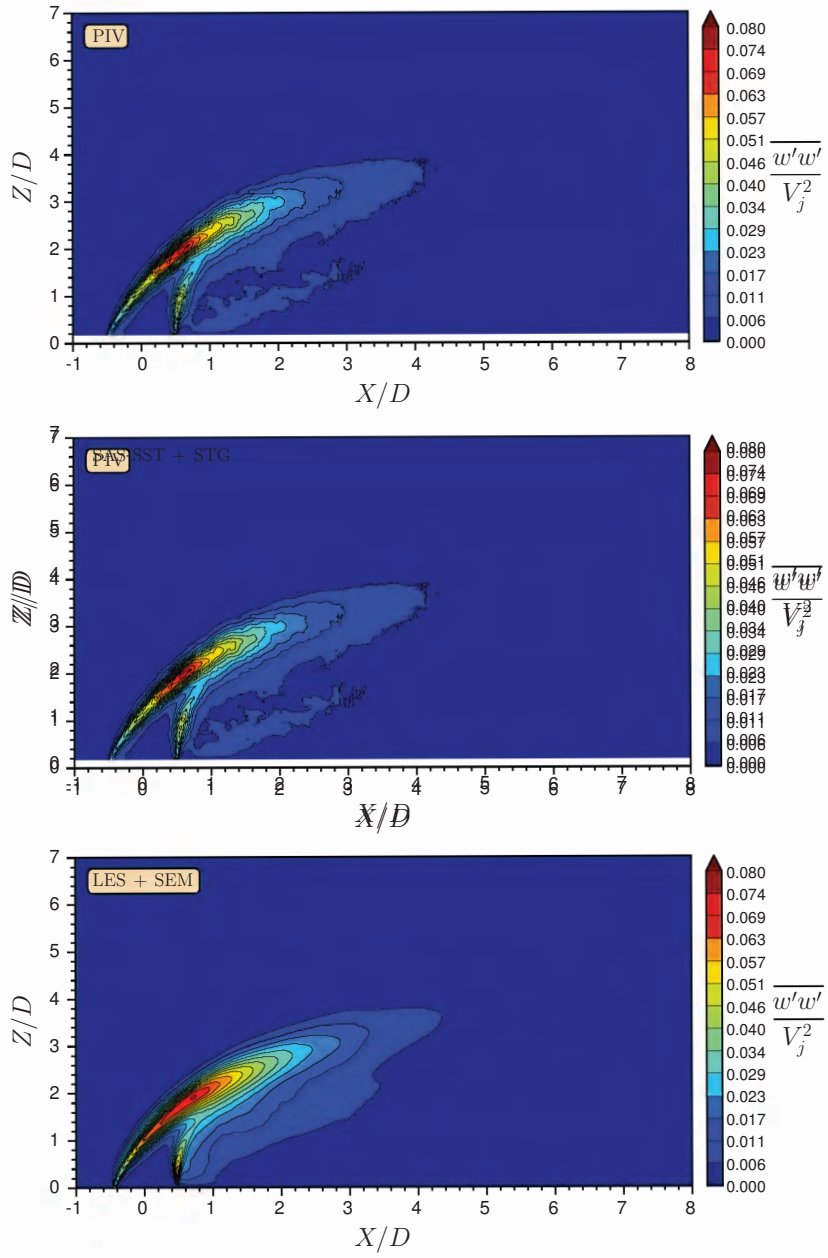

Figure 15: Reynolds normal stress $\overline{w'w'}$ field in the centreplane $Y/D = 0$ normalized by squared jet velocity V_j^2. From top to bottom: PIV measurements, SAS-SST + STG and LES + SEM.

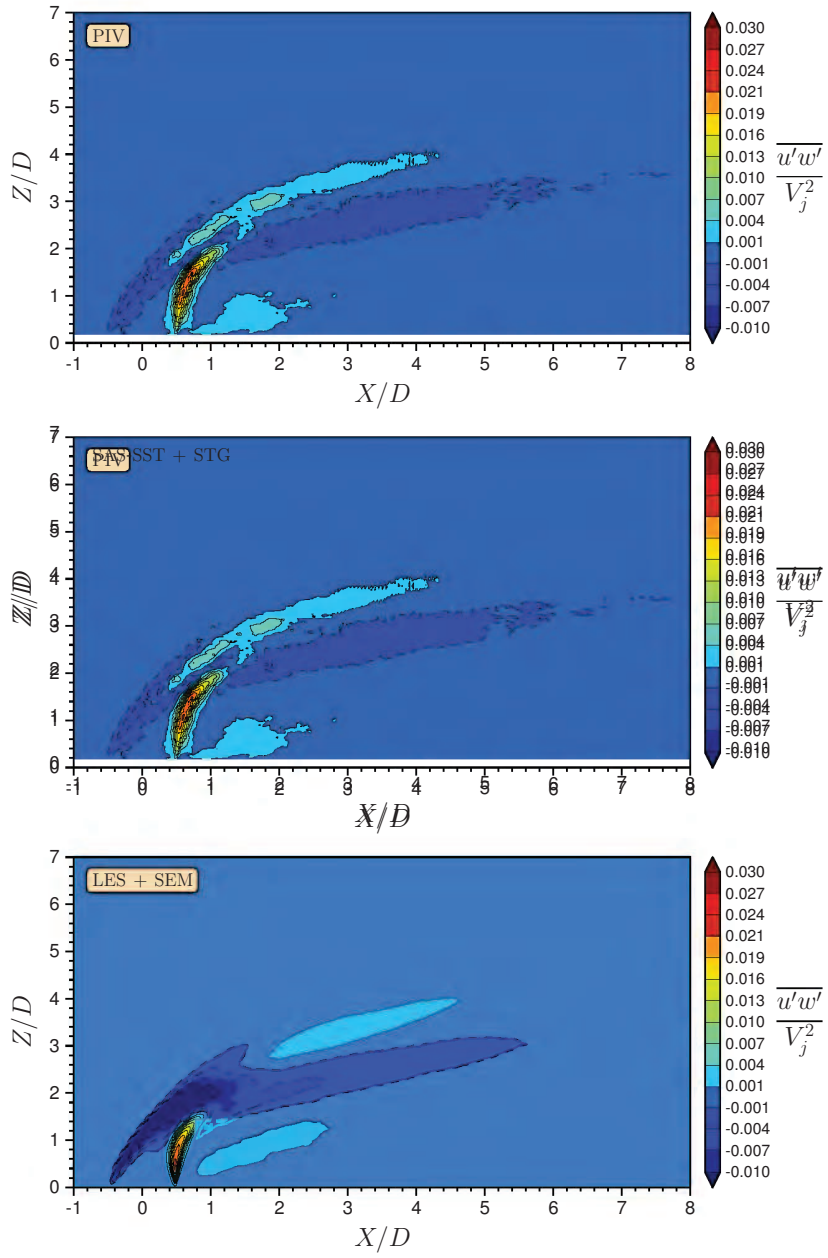

Figure 16: Reynolds shear stress $\overline{uw}$ field in the centreplane $Y/D = 0$ normalized by squared jet velocity V_j^2. From top to bottom: PIV measurements, SAS-SST + STG and LES + SEM.

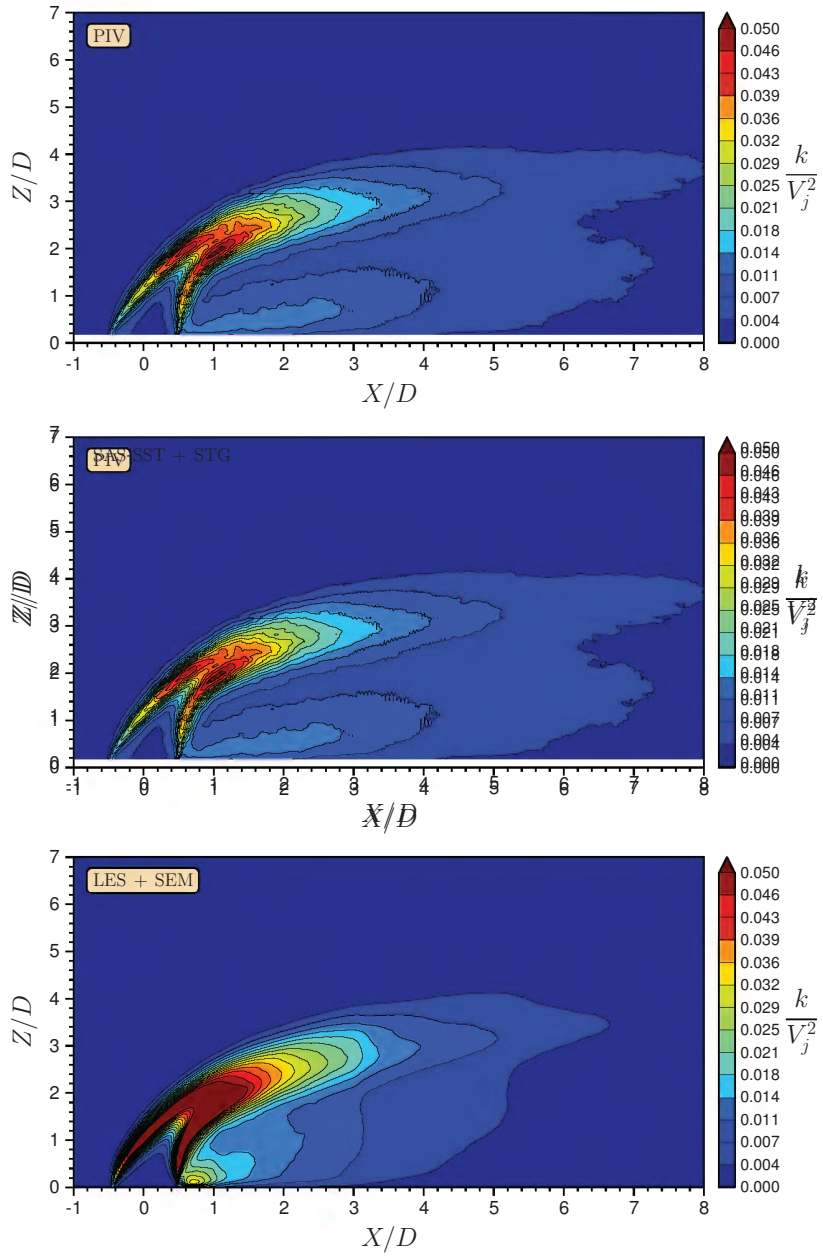

Figure 17: Turbulent kinetic energy k field in the centreplane $Y/D = 0$ normalized by squared jet velocity V_j^2. From top to bottom: PIV measurements, SAS-SST + STG and LES + SEM.

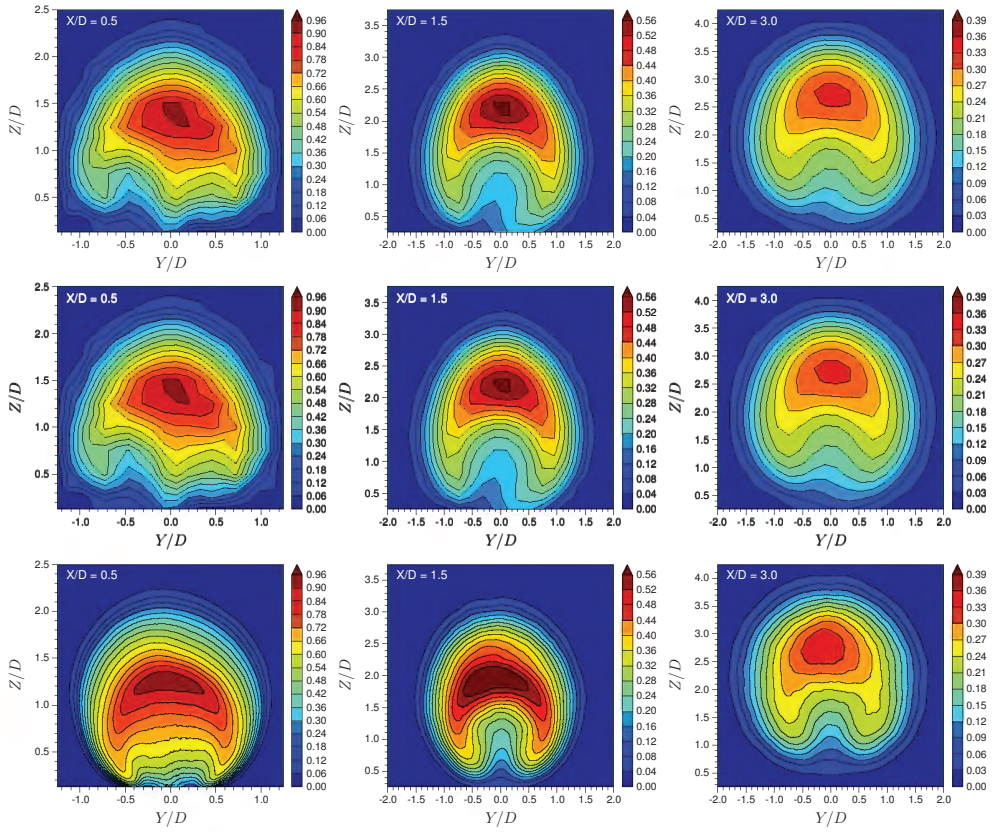

Figure 18: Normalized mean static temperature fields $\theta = (T - T_{cf})/(T_j - T_{cf})$ in three transverse planes (from left to right: $X/D = 0.5$, 1.5 and 3.0). Thermocouples measurements (top), SAS-SST + STG (middle) and LES + SEM (bottom).

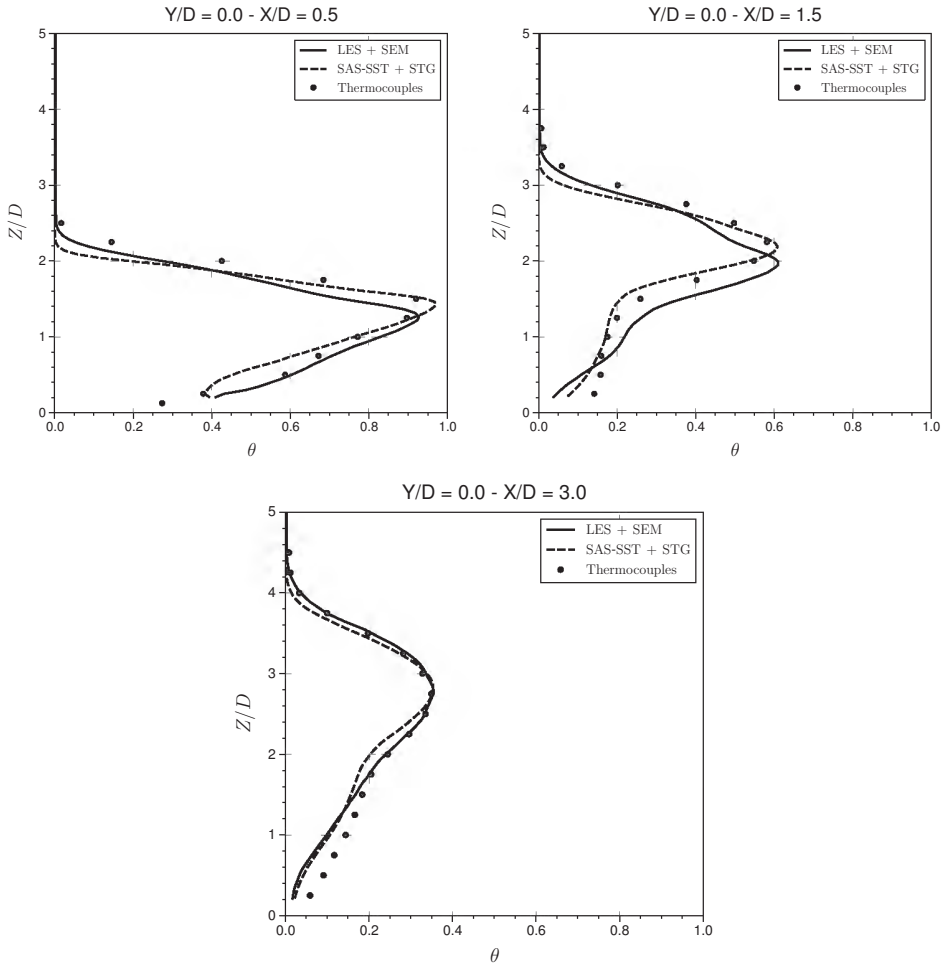

Figure 19: Normalized mean static temperature $\theta = (T - T_{cf})/(T_j - T_{cf})$ profiles in the centreplane at three downstream locations ($X/D = 0.5$, 1.5 and 3.0).

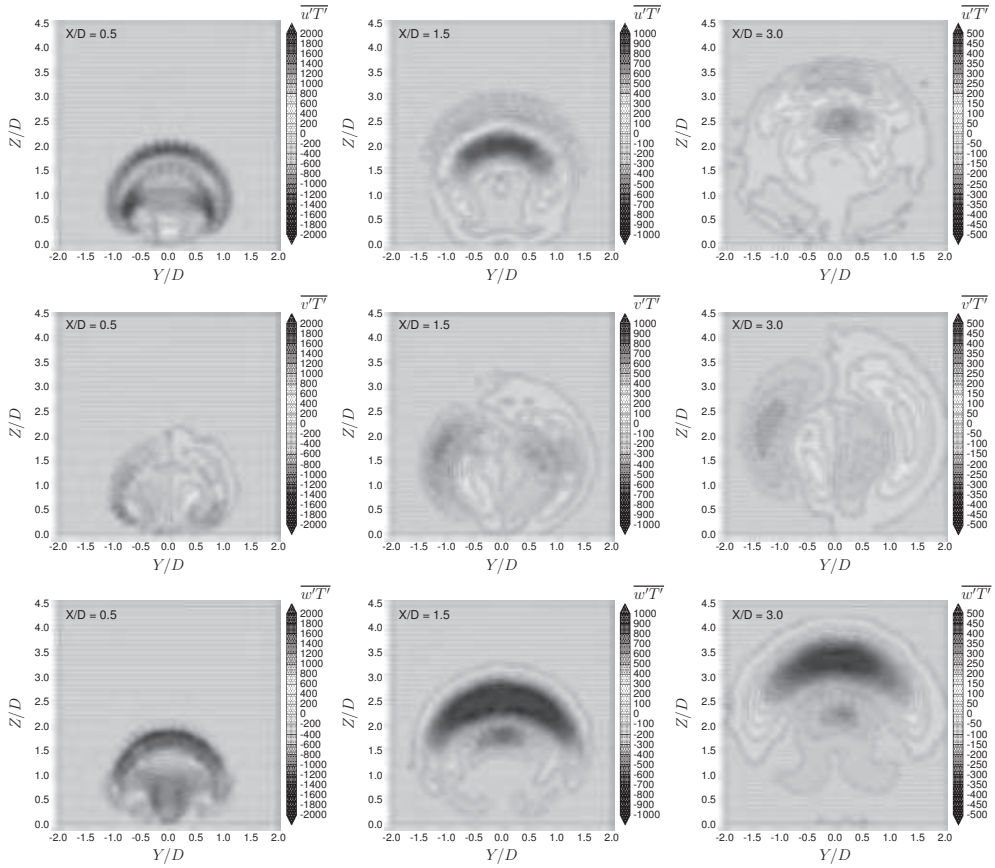

Figure 20: Contour plots of the three components of the time-resolved turbulent heat flux vector in three transverse planes (from left to right: $X/D = 0.5$, 1.5 and 3.0). SAS-SST + STG simulation results: $\overline{u'T'}$ (top), $\overline{v'T'}$ (middle) and $\overline{w'T'}$ (bottom).

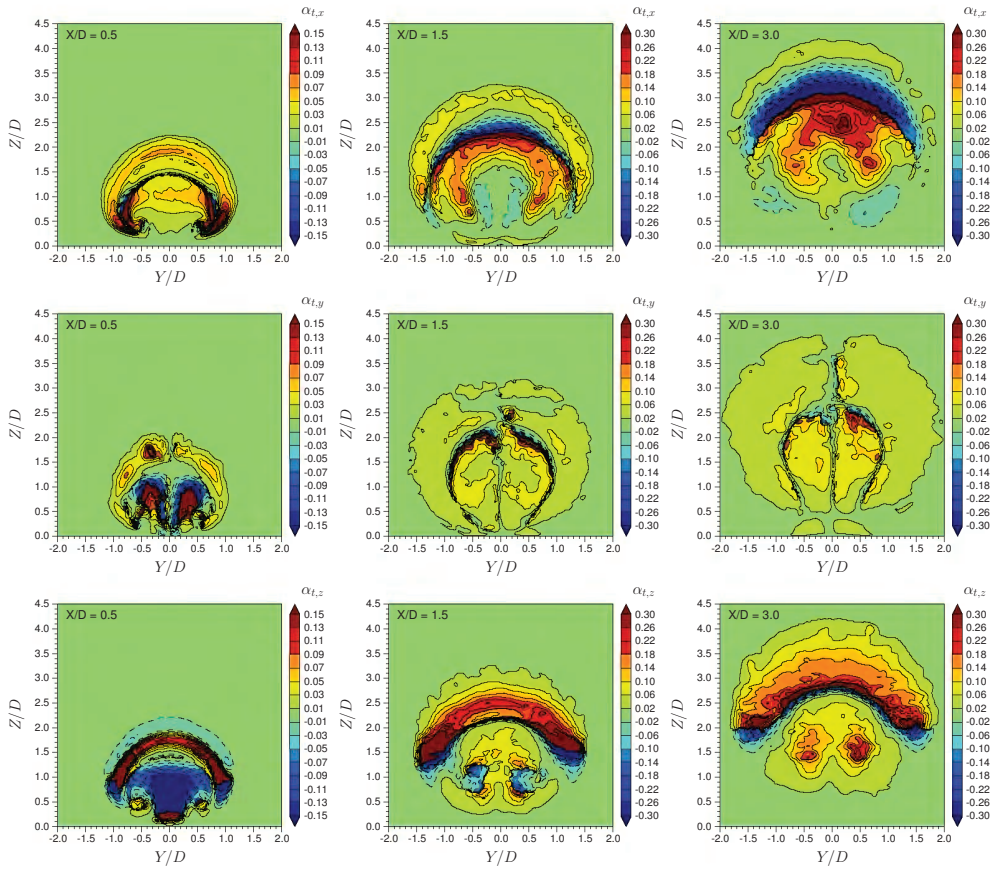

Figure 21: Contour plots of the three components of the turbulent diffusivity α_t in three transverse planes (from left to right: $X/D = 0.5$, 1.5 and 3.0). SAS-SST + STG simulation results: $\alpha_{t,x}$ (top), $\alpha_{t,y}$ (middle) and $\alpha_{t,z}$ (bottom).

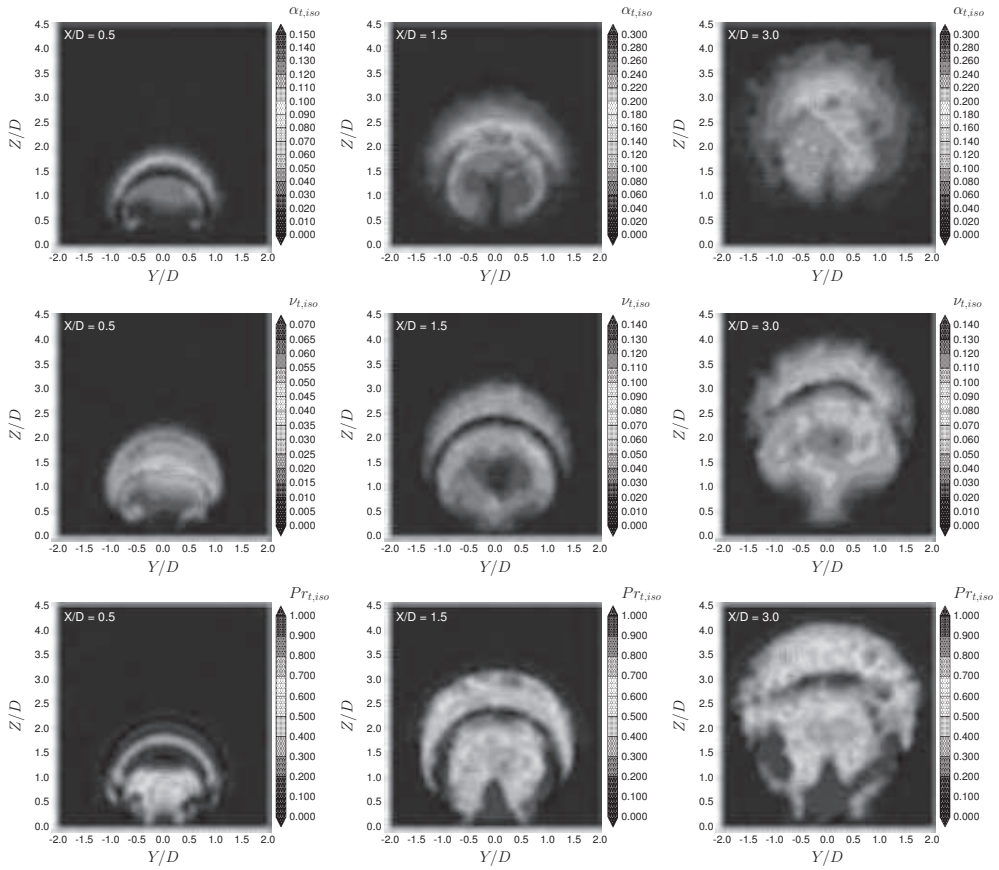

Figure 22: Contour plots of the isotropics turbulent diffusivity $\alpha_{t,iso}$ (top), eddy viscosity $\nu_{t,iso}$ (middle) and turbulent Prandtl number $Pr_{t,iso}$ computed from the SAS-SST + STG results in three transverse planes (from left to right: $X/D = 0.5$, 1.5 and 3.0).

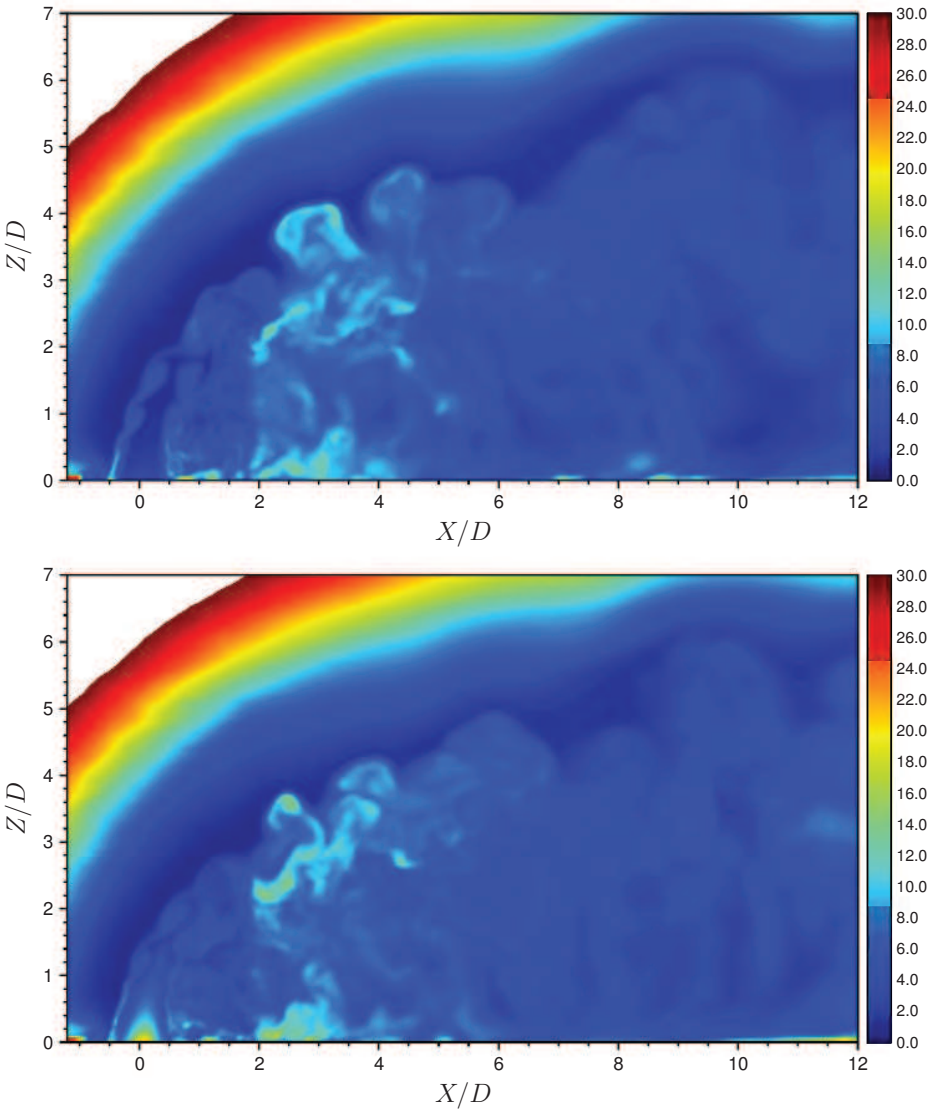

Figure 23: Influence of synthetic turbulence injection at the pipe inlet on viscosity ratio ν_t/ν levels in the centreplane $Y/D = 0$. SAS-SST + STG (top) and SAS-SST (bottom).

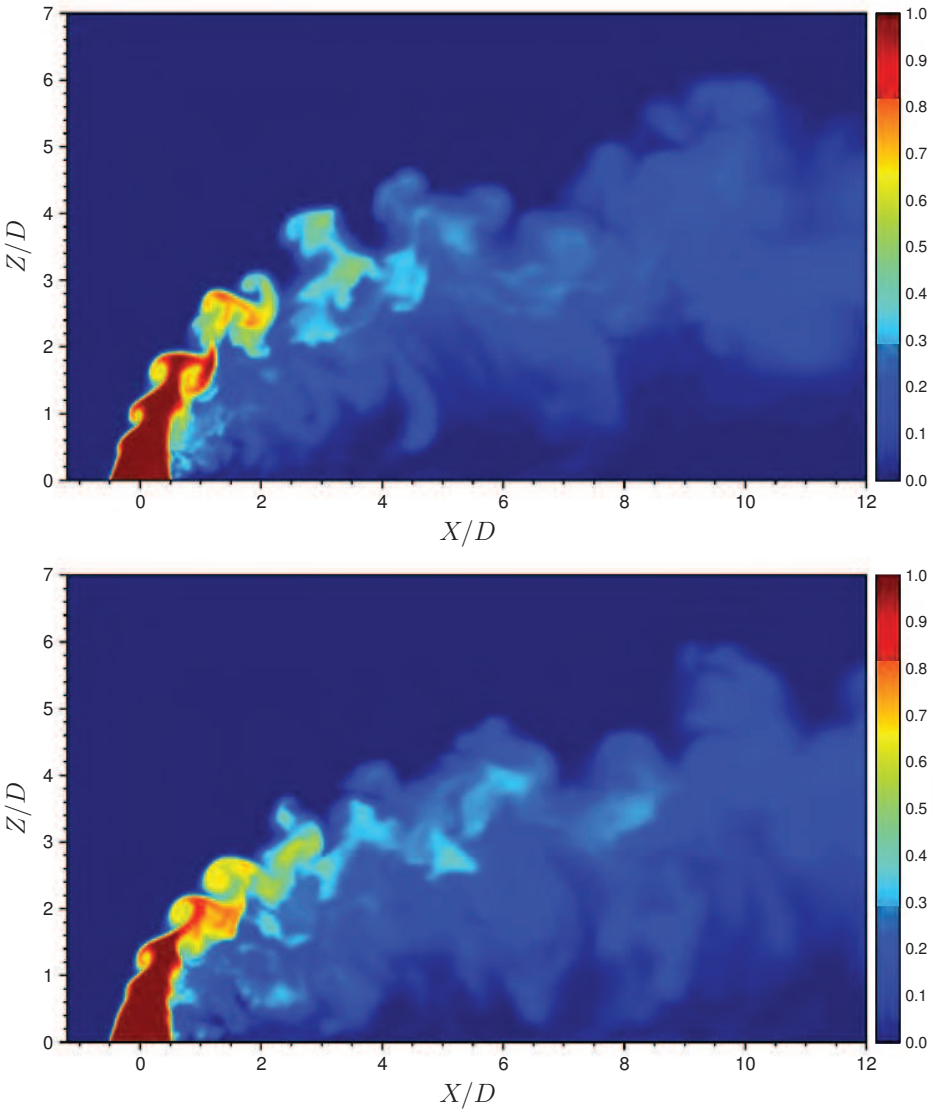

Figure 24: Instantaneous fields of normalized temperature $\theta = (T - T_{cf})/(T_j - T_{cf})$ in the centreplane $Y/D = 0$. SAS-SST + STG (top) and SAS-SST (bottom).

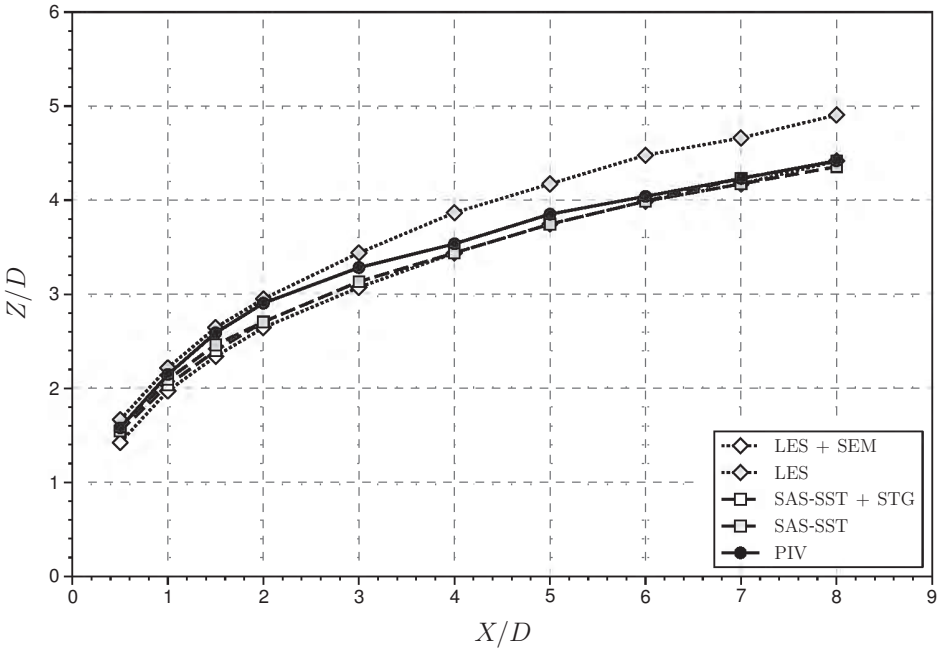

Figure 25: Jet trajectories based on local mean longitudinal velocity U maxima in the centreplane $Y/D = 0$. Influence of synthetic turbulence injection at the pipe inlet.

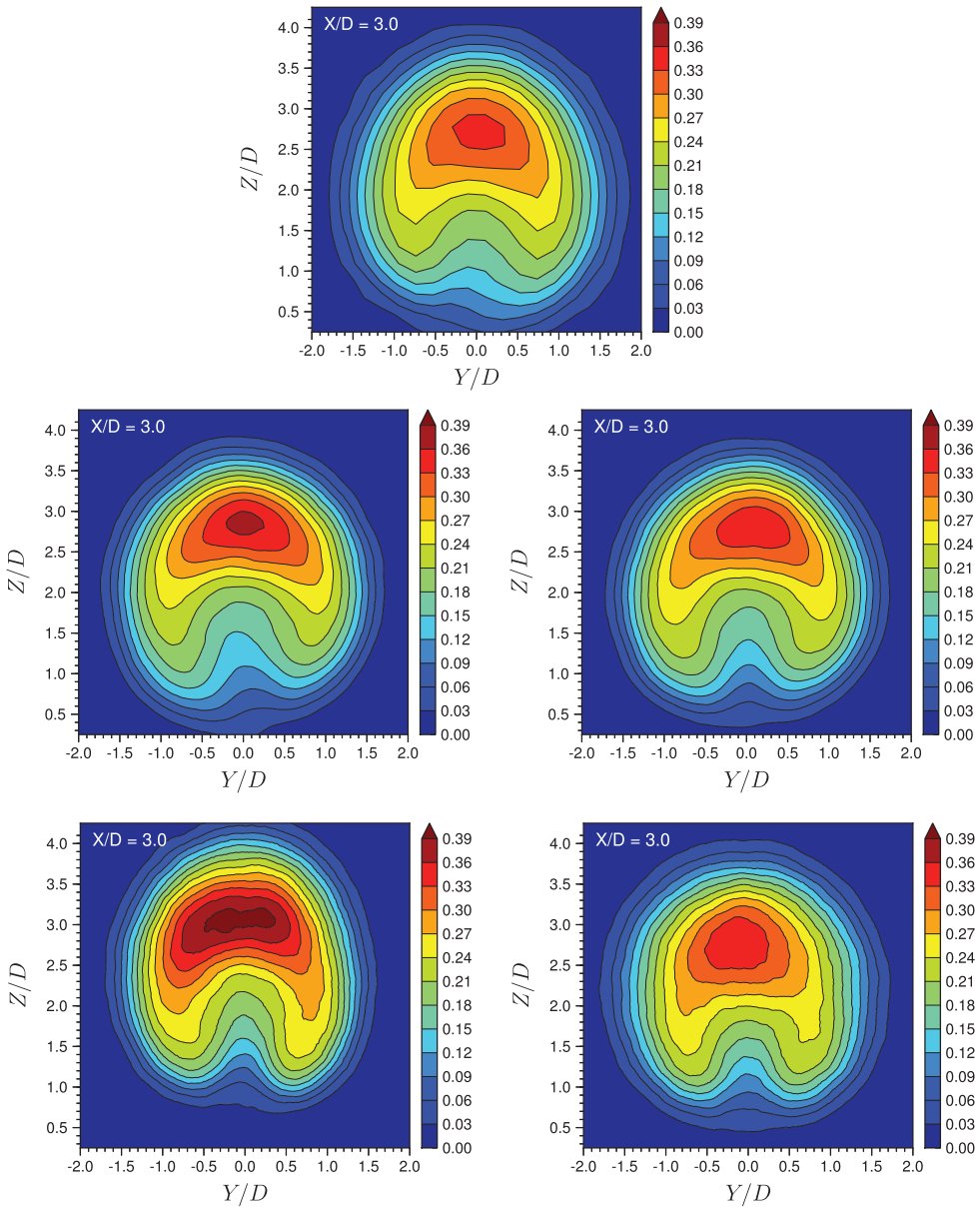

Figure 26: Normalized mean static temperature fields $\theta = (T - T_{cf})/(T_j - T_{cf})$ in the transverse plane located at $X/D = 3.0$. Thermocouples measurements (top), SAS-SST (middle left), SAS-SST + STG (middle right), LES (bottom left) and LES + SEM (bottom right).